Evaluation and Validation of HF Radar Swell and Wind-Wave Inversion Method

ZAID R. AL-ATTABI,[a,b,c] GEORGE VOULGARIS,[a] AND DANIEL C. CONLEY[d]

[a] *School of the Earth, Ocean and Environment, University of South Carolina, Columbia, South Carolina*
[b] *Marine Science Center, University of Basrah, Basrah, Iraq*
[c] *Department of Coastal Studies, East Carolina University, Wanchese, North Carolina*
[d] *School of Biological and Marine Sciences, Plymouth University, Plymouth, United Kingdom*

(Manuscript received 15 November 2020, in final form 13 July 2021)

ABSTRACT: An examination of the applicability and accuracy of the empirical wave inversion method in the presence of swell waves is presented. The ability of the method to invert Doppler spectra to wave directional spectra and bulk wave parameters is investigated using 1-month data from a 12-MHz Wellen Radar (WERA) high-frequency (HF) radar system and in situ data from a wave buoy. Three different swell inversion models are evaluated from Lipa et al. (LPM), from Wang et al. (WFG), and empirical (EMP), an empirical approach introduced in this study. The swell inversions were carried out using two different scenarios: 1) a single beam from a single radar site and two beams from a single radar site, and 2) two beams from two sites (a single beam per site) intersecting each other at the buoy location. The LPM method utilizing two beams from two different sites was found to provide the best estimations of swell parameters (swell height RMS error: 0.24 m) and showed a good correlation with the partitioned swell in situ values. For the wind-wave inversion, the empirical method presented here is used with an empirical coefficient of 0.3, which seems to be suitable for universal application for all radar operating frequencies. The inverted swell parameters are used to create a swell spectrum that is combined with the inverted wind-wave spectrum to create a full directional wave spectrum. The wave inversion method presented in this study although empirical does not require calibration with in situ data and can be applied to any beam-forming system and operating frequency.

KEYWORDS: Ocean; Gravity waves; Waves, oceanic; Wind waves; Inversions; Algorithms; Buoy observations; Data processing; Data quality control; In situ oceanic observations; Measurements; Radars/Radar observations; Regression analysis; Sea/ocean surface; Sea state; Remote sensing

1. Introduction

Doppler energy spectra estimated from electromagnetic (EM) waves backscattered from the ocean surface (Crombie 1955) contain information on both surface currents and ocean waves. The first-order spectral peaks are due to backscatter by ocean waves with a wavelength half the EM wave wavelength; the shift from the theoretical Bragg frequency is used to estimate the ocean surface current along the direction of the beam (radial currents; e.g., Paduan and Rosenfeld 1996). The spectral continuum present on either side of each first-order Bragg peak (second-order scattering) is the result of nonlinear interactions between the EM waves and a combination of ocean surface waves that satisfy the requirement that the sum of their wavenumber vectors equals that of the Bragg wave (i.e., Stewart 1971; Hasselmann 1971; Weber and Barrick 1977). This continuum is referred to as the second-order sideband spectrum and it contains the signature of the ocean waves present at the surface of the ocean.

The relationship between ocean waves and high-frequency (HF) radar Doppler spectra has been described theoretically in Barrick (1971) and Barrick and Weber (1977), and it has been utilized (Barrick 1977b) to develop an inversion technique for estimating ocean waves from the Doppler spectrum. Lipa (1977) linearized Barrick's equations and used a stabilization technique to carry out the inversion of a theoretical wave spectrum. Subsequently, several other inversion methods were developed that included the application of singular value decomposition (SVD) techniques (i.e., Gill 1990; Howell and Walsh 1993; Zhang and Gill 2006) for bistatic radar systems, the Chahine–Twomey relaxation method (Wyatt 1990), or provided direct solutions of the nonlinear integral equations (Hisaki 1996). However, the simpler empirical method of Barrick (1977a,b) has been the basis for a number of wave inversions of HF radar Doppler spectra, including those described in Maresca and Georges (1980) and Heron et al. (1985). Gurgel et al. (2006) extended the empirical algorithm to allow for the estimation of wave directional characteristics using the Doppler spectra from two phased array HF radars located at different locations along the coast. Lopez et al. (2016) evaluated the method of Gurgel et al. (2006) and noted that the empirical coefficients required by that method were different than those suggested by Gurgel et al. (2006) even after adjusting for differences in operating frequency.

Although these studies focused on wind-wave inversion, discrepancies were found when swell waves were present (e.g., Shen et al. 2012; Lopez et al. 2016; Essen et al. 1999; Gurgel et al. 2006; Gomez et al. 2015; Wyatt 1986, 2002, 1999; Heron and Prytz 2002). Lipa and Barrick (1980) showed that the extraction of swell information from Doppler spectra is different

Al-Attabi's current affiliation: Department of Coastal Studies, East Carolina University, Wanchese, North Carolina.

Corresponding author: Zaid R. Al-Attabi, zrahman@geol.sc.edu

DOI: 10.1175/JTECH-D-20-0186.1

from that developed for wind waves. Lopez et al. (2016) noted that the amplitude of the empirical calibration coefficients varied significantly at low wave frequencies ($f < 0.12$ Hz) and this variability was dependent on the angle between the direction of swell propagation and radar beam (swell cross angle). Higher values were estimated for cases when the swell cross angle was close to 90°, while the values were reduced for smaller swell cross angles. Similar directional dependence was also reported earlier in Lipa and Barrick (1980) and wave inversions using both theoretical (Wyatt 1999) and empirical (Gurgel et al. 2006) methods.

More recently, Alattabi et al. (2019) used a hybrid empirical inversion technique that combines Barrick's (1977b) original wind-wave inversion method and a simplified swell inversion method to reconstruct the wave spectrum from a very high-frequency (VHF, 48 MHz) radar system. In their study, it was shown that the regression coefficient for wind-wave inversion was not wave frequency dependent as suggested by Gurgel et al. (2006) and Lopez et al. (2016); an almost constant value was proposed that was similar to that found in the studies of Ramos et al. (2009) and Heron and Heron (1998) who used different frequency radar systems. These findings suggested a universal application of the empirical inversion method that if true, makes in situ calibration redundant. However, in Alattabi et al. (2019) the swell inversion assumed no directional dependence, mainly due to the short ranges and shallow water depths the data corresponded to. At such shallow depths, the swell crests are almost parallel to the coastline due to wave refraction and there is minimal directional variability; these conditions allowed for the adoption of an empirically defined, non-directional-dependent coefficient for the estimation of swell wave height.

This study extends the hybrid empirical method of Alattabi et al. (2019) for swell conditions of variable directionality and tests its universality using a radar system of different frequency (12 MHz) than that used in the original study (48 MHz). The hypothesis is that if the empirical coefficient for the wind-wave inversion module is similar to that obtained using the 48-MHz system then the module is universally applicable. The extension of the model for variable swell conditions is carried out by evaluating the performance of the swell inversion methods of Lipa et al. (1981) and Wang et al. (2016) and comparing it against an expanded form of the simplified parameterization used in Alattabi et al. (2019) that allows for swell directionality.

In this manuscript, section 2 describes briefly the theoretical swell inversion models presented elsewhere and presents the development of the expanded empirical method of Alattabi et al. (2019) for swell and wind-wave (empirical) inversions. Section 3 presents the data used to evaluate the inversion models described in section 2, while the methodology used is described in section 4. Section 5 presents the swell inversion results, and in section 6 the findings are discussed in detail. Finally, the conclusions of the study are presented in section 7.

2. Inversion models

a. Theoretical swell inversion model

Lipa and Barrick (1980) described in detail methods for extracting long (swell) wave information from second-order Doppler spectra derived from HF radars. Later, Lipa et al. (1981) evaluated

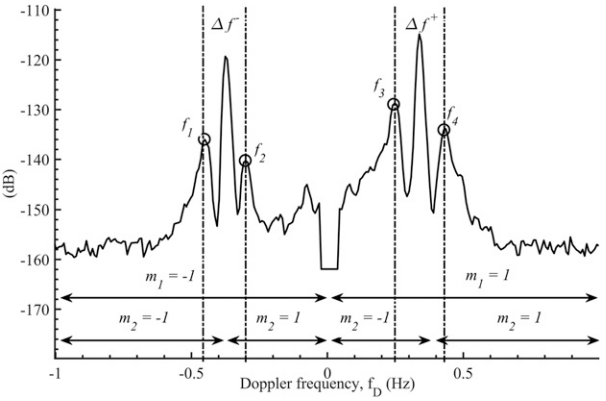

FIG. 1. Example of HF radar Doppler backscatter spectrum obtained from the HF radar (12 MHz) used in this study. The locations of the four peaks (f_1 to f_4) due to swell waves are shown. The horizontal lines denote the regions of the Doppler spectra that the values of m_1 and m_2 correspond to [see Eq. (1)].

these methods using sea-echo data from a narrow beam HF radar system on the Pacific Ocean. In their study, they used swell conditions of varying complexity including monochromatic, unidirectional with a directional spread, and combination of two monochromatic swell systems. If a monochromatic swell (i.e., single direction and frequency (f_s) is present, then four peaks appear on the Doppler spectrum at frequencies (f_{Dj}) given by

$$f_{Dj} = m_1(f_B^4 + f_s^4 + 2m_2 f_s^2 f_B^2 \cos\theta_s)^{1/4} + m_2 f_s, \qquad (1)$$

where θ_s is the swell propagation direction with respect to the radar beam direction (i.e., swell cross angle); ihe index j (=1 to 4) defines the position of the peak within the region of the Doppler spectrum (from left to right), which in turn is defined by the parameters m_1 and m_2 [i.e., j = 1, 2, 3 and 4 when (m_1, m_2) = (−1, −1), (−1, 1), (1, −1), and (1, 1), respectively, see Fig. 1 for details]; and f_B is the frequency of the first-order Bragg peak identified in the Doppler spectrum (including currents).

Equation (1) allows for the estimation of the swell cross angle using

$$\theta_s = \cos^{-1}\left[\frac{8f_B(\Delta f^+ - \Delta f^-)}{(\Delta f^+ + \Delta f^-)^2}\right], \qquad (2)$$

where Δf is the frequency separation (distance) between the swell-induced Doppler peaks around the positive ($\Delta f^+ = f_{D4} - f_{D3}$) and negative ($\Delta f^- = f_{D2} - f_{D1}$) Bragg peaks (see Fig. 1). Swell direction (θ_{sw}) is then estimated as $\theta_{sw} = \theta_r - \theta_s$, where θ_r is the radar beam direction. The frequency of the swell is estimated as

$$f_s = \frac{\Delta f^+ + \Delta f^-}{4}, \qquad (3)$$

and assuming deep-water conditions the wavenumber is given by

$$k_{so} = (2\pi)^2(\Delta f^+ + \Delta f^-)^2/16g. \qquad (4)$$

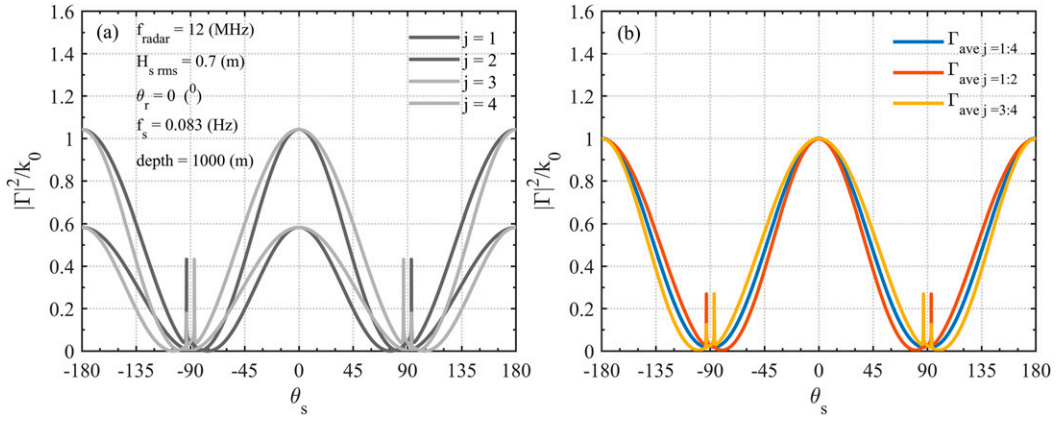

FIG. 2. (a) Variability of normalized coupling coefficient for each swell peak around the Bragg peaks (j = 1 to 4; gray lines) as a function of swell cross angle. (b) Variability of various combinations of averages using the values shown on the left: (i) average of all four coefficients (j = 1:4, in blue); (ii) average of the two coupling coefficients corresponding to the negative (j = 1:2, in red) and positive (j = 3:4, in orange) sides of the Doppler spectrum.

For any arbitrary depth h the swell wavenumber k_s is related to the deep-water wavenumber through (Phillips 1966)

$$k_s = k_{so}\tanh(k_{so}h). \tag{5}$$

Based on Lipa and Barrick (1980) the root-mean-square (RMS) swell wave height can be obtained from each side of the Doppler spectrum using the ratio $\mathcal{R}_j = \sigma_2(f_{Dj})/\sigma_1(f_{Bm_1})$, where $\sigma_2(f_{Dj})$ is the second-order Doppler spectral energy level corresponding to the swell peak and $\sigma_1(f_{Bm_1})$ is the adjacent first-order Bragg peak (i.e., $m_1 = -1$ for j = 1 or 2 and $m_1 = 1$, for j = 3 or 4, see Fig. 1) so that

$$H_{\rm sw}^2 = \frac{\mathcal{R}_j}{2|\Gamma_j(k_s,\theta_s)|^2 C_j}; \tag{6}$$

$\Gamma_j(k_s, \theta_s)$ in Eq. (6) is the coupling coefficient that represents the hydrodynamic and electromagnetic interaction of the electromagnetic wave with the ocean waves at each region (defined by j) of the Doppler spectrum; and C_j is a residual term related to the background wind-wave field. Lipa et al. (1981) and Lipa and Barrick (1980) assumed $C_j = 1$, while Wang et al. (2016), using a Pierson–Moskowitz wave spectrum to describe the background wind waves, suggested that C_j is approximated as

$$C_j \approx [1 + (k_s/k_o)^2/4 + m_1 k_s \cos\theta_s/k_o]^{-2}, \tag{7}$$

where θ_s is the swell cross angle, and k_s and k_o are the swell and radar wavenumbers, respectively. The value of $m_1 = \pm 1$ depends on the region of the Doppler spectrum the swell peak is located (i.e., $m_1 = -1$ for j = 1, 2 and $m_1 = 1$ for j = 3, 4, see Fig. 1).

The coupling coefficient Γ_j (k_s, θ_s) in Eq. (6) can be estimated (see appendix A in Wang et al. 2016) for each region j of the Doppler spectrum and any depth h as the sum of the electromagnetic and hydrodynamic coefficients (see Fig. 2).

Application of the model described by Eqs. (2) and (3) (herein referred to as LPM1) requires identification of all four swell peaks from both sides of a single Doppler spectrum. When only two swell peaks, from one side of the spectrum, are identifiable then two beams from two different radar sites (i.e., different cross angles) can be used. Following Lipa et al. (1981), if the angle between the two beams is ϕ, then the Doppler frequencies corresponding to the swell peaks are given by

$$f_{Dj}^{b_1} = m_1(f_{Bj}^4 + f_s^4 + 2m_2 f_s^2 f_B^2 \cos\theta_s)^{1/4} + m_2 f_s \tag{8}$$

and

$$f_{Dj}^{b_2} = m_1[f_{Bj}^4 + f_s^4 + 2m_2 f_s^2 f_B^2 \cos(\theta_s + \phi)]^{1/4} + m_2 f_s \tag{9}$$

for beams b_1 and b_2, respectively. In this case the swell cross angle (θ_s) above is defined with reference to beam b_1.The normalized second-order energy at the corresponding swell peak and beam are

$$R_j^{b_1} = 2H_{\rm sw}^2|\Gamma_j^{b1}(k_s,\theta_s)|^2 \tag{10}$$

and

$$R_j^{b_2} = 2H_{\rm sw}^2|\Gamma_j^{b2}(k_s,\theta_s+\phi)|^2. \tag{11}$$

In this case, as suggested by Lipa et al. (1981) and later discussed by Shen et al. (2012), estimates of swell frequency (f_s) and cross angle (θ_s) are obtained using Eqs. (8) and (9) through a least squares minimization method, while swell height ($H_{\rm sw}$) and cross angle (θ_s) are obtained using Eqs. (10) and (11).

The same approach [i.e., Eqs. (8)–(11)] could be implemented using two beams from a single radar site, as in Lipa et al. (1981). However, in the latter case the angle between the two beams should be at least 2 times greater than the beamwidth as to ensure that the corresponding Doppler spectra are independent from each other and represent different patches of the ocean surface (Voulgaris et al. 2011). However, this approach assumes that the swell conditions are similar at the

two locations, an assumption that might be violated especially for longer ranges as the two beams look at different areas of the ocean. Despite this weakness this method might be the only option available when data from only one HF radar is available. Hereafter, this method (i.e., use of two beams) is referred to as the LPM2$_i$ method, with the subscript i denoting the number of sites used (i.e., LPM2$_1$ denotes application using two beams from a single site while LPM2$_2$ indicates use of two beams from two different sites, for more details see section 4).

More recently Wang et al. (2016) presented a swell inversion method that uses Eq. (3) for obtaining f_s and a least squares method to minimizes the difference (Q) between the theoretical ($\mathcal{R}_j$) and measured (R_j) swell peaks:

$$Q = \sum_{j=1:4} (\mathcal{R}_j - R_j)^2. \tag{12}$$

The RMS swell wave height is obtained by setting $\partial Q/\partial H_{\rm sw} = 0$, so that

$$H_{\rm sw}^2 = \frac{4\sum_{j=1:4} R_j |\Gamma_j(k_s,\theta_s)|^2 C_j}{\sum_{j=1:4} |\Gamma_j(k_s,\theta_s)|^4 C_j^2}. \tag{13}$$

The swell cross angle is estimated by substituting Eq. (13) into Eq. (6) for use in Eq. (12), which then becomes a function of the cross angle (θ_s) only. The latter is defined as the value for which $Q(\theta_s)$ is minimized.

The method of Wang et al. (2016) described above (herein referred to as the WFG1 method) requires information from both sides of the Doppler spectrum. In the case where only one side of the Doppler spectrum is available, the method can be modified for use with two beams (b_1 and b_2) obtained from two different radar systems or from two beams from a single site as described earlier. In this case

$$H_{\rm sw}^2 = \frac{4\sum_j R_j^{b_1} |\Gamma_j^{b_1}(k_s,\theta_s)|^2 C_j^{b_1} + \sum_j R_j^{b_2} |\Gamma_j^{b_2}(k_s,\theta_s+\phi)|^2 C_j^{b_2}}{\sum_j |\Gamma_j^{b_1}(k_s,\theta_s)|^4 C_j^{b_1^2} + \sum_j |\Gamma_j^{b_2}(k_s,\theta_s+\phi)|^4 C_j^{b_2^2}}, \tag{14}$$

where the superscripts b_1 and b_2 denote the two different beams (with b_1 being the reference beam) and ϕ is the angle between them. Swell direction and frequency are estimated using Eqs. (8) and (9) as in Lipa et al. (1981). The wave height is calculated using Eq. (14) and a second solution for swell direction is obtained as before by minimizing $Q(\theta_S)$. This method is referred to as the WFG2$_i$ method, with the subscript i denoting the source of the two beams (i.e., from a single or two different HF radar sites) as described earlier.

b. *Empirical swell inversion model*

The models described above [also see Lipa and Barrick (1980) and Bathgate et al. (2006)] indicate a strong relationship between swell height and the coupling coefficient; the latter has a strong directional dependence that is shown to be related to cos^2 of the swell cross angle (θ_s) [see appendix A in Lipa and Barrick (1980)]. As an example, the magnitude of the coupling coefficient $|\Gamma|^2$ for a 0.083 Hz swell and a radar frequency of 12 MHz is shown in Fig. 2. As Lipa and Barrick (1980) and Bathgate et al. (2006) have shown, this directional dependence leads to singularities at high swell cross angles ($\approx$90°) that make swell inversion impossible (see Fig. 2 at angles near ±90°).

In the empirical model of Alattabi et al. (2019) this directional dependence was not considered and an empirically defined coefficient α_s was used to estimate the swell wave height so that

$$H_{\rm sw}^2 = \alpha_s \frac{2R_s}{k_o^2}, \tag{15}$$

where $R_s = \sum_j R_j$, with j denoting the number of swell peaks identified (2 or 4 depending on the quality of the Doppler spectra), and k_o is the radar wavenumber. This assumption of no directional dependence was justified by the very shallow water depths (~5–10 m) that ensured an almost constant swell angle of approach due to wave refraction (see Alattabi et al. 2019).

If we relax this assumption, then swell direction estimations can be obtained using Eqs. (8) and (9) presented earlier. Alternatively, the method of Gurgel et al. (2006) can be utilized. This empirical method assumes a direct relationship of the swell wave directional distribution function $F(\varphi)$ to the ratio of swell peaks around the dominant Bragg peak {$\gamma_s = \sigma_2(f_3)/\sigma_2(f_1)$ or $\sigma_2(f_4)/\sigma_2(f_2)$ or $[\sigma_2(f_3)+\sigma_2(f_4)]/[\sigma_2(f_1)+\sigma_2(f_2)]$}, for the positive and negative Doppler frequencies of the spectrum. The inverted swell cross-angle direction is then estimated using the ratio from beam 1 ($\gamma_s^{b_1}$) and beam 2 ($\gamma_s^{b_2}$) by minimizing the following function:

$$Q = \left[\gamma_s^{b_1} - \frac{F(\varphi-\theta_{r_1})}{F(\varphi-\theta_{r_1}+\pi)}\right]^2 + \left[\gamma_s^{b_2} - \frac{F(\varphi-\theta_{r_2})}{F(\varphi-\theta_{r_2}+\pi)}\right]^2, \tag{16}$$

where F [=cos^2(0.5θ)] is the directional distribution function used in this study; θ_{r_1} and θ_{r_2} are the beam angles from beams (or sites) 1 and 2. It should be noted that Gurgel et al. (2006) used F [=sech$^2(\cdot)$] as to avoid singularities at high swell cross angles. This certainly is an option but a comparison of the two distributions lead to only a slight improvement for a limited number of cases (<5%). For consistency, in this paper we have maintained the cos^2 distribution although the code allows the inclusion of any function. The value of φ that minimizes Q is considered to correspond to the inverted swell direction θ_{sw}. Once swell direction is estimated using Eq. (16) the simple swell model of Alattabi et al. (2019) can be expanded to allow for changes in swell wave cross angle. This modification makes the empirical coefficient shown in Eq. (15) to be dependent on the swell cross angle. When averaging all coupling coefficients corresponding to the individual second-order swell peaks, the variation of the mean of $|\Gamma|^2$ (see Fig. 2 right panel) can be empirically expressed as

$$\overline{\Gamma}_j(k_s,\theta_s) = \overline{A}_j(k_s)\cos^n(\theta_s), \tag{17}$$

where the overbar denotes averaged values and A_j is the maximum value for each coupling coefficient j. Based on Eq. (17) the empirical coefficient α_s in Eq. (15) can be substituted by $\alpha_s/\cos^n(\theta_s)$ so that

$$H_{sw}^2 = \frac{2\alpha_s}{k_o^2 \cos^n\theta_s} \sum_j R_j, \tag{18}$$

where $\alpha_s = 1/\overline{A_j}(k_s)$, and the value of n (see Fig. 2) depends on the Doppler spectrum side used (see Fig. 2 right panel).

A theoretical examination of A_j and n for a large range of radar frequencies (4–48 MHz) and swell wavelengths was carried out (not shown here) and showed that when both sides of the Doppler spectrum are used (i.e., $j = 1, 2, 3, 4$) then $n = 2.02$, $\alpha_s = 1.18$. This method is denoted as EMP1; and it can be utilized using two beams from two sites ($EMP2_2$) or a single radar ($EMP2_1$). In this case Eq. (18) can be written as

$$H_{sw}^2 = \frac{2\alpha_s}{k_o^2 \cos^n(\theta_s)} \sum_{j=1,2/3,4} R_j^{b_1}, \tag{19}$$

$$H_{sw}^2 = \frac{2\alpha_s}{k_o^2 \cos^n(\theta_s + \phi)} \sum_{j=1,2/3,4} R_j^{b_2}, \tag{20}$$

where $n = 2.25$ and $\alpha_s = 0.98$ for $j = 1, 2$ and $n = 2.10$, and $\alpha_s = 1.45$ for $j = 3, 4$. As before, b_1 and b_2 denote the two beams and the swell cross angle (θ_s) is measured from beam b_1. The average value of H_{sw}^2 from Eqs. (19) and (20) is used to estimate swell wave height, while the swell frequency using $EMP2_2$ and $EMP2_1$ is estimated as

$$f_s = \frac{(\Delta f_{b_1}^-)_{j=1,2} + (\Delta f_{b_2}^+)_{j=3,4}}{4} \quad \text{or} \quad \frac{(\Delta f_{b_1}^+)_{j=3,4} + (\Delta f_{b_2}^-)_{j=1,2}}{4}. \tag{21}$$

c. Wind-wave inversion model

The empirical wind-wave inversion method used in Alattabi et al. (2019) is based on Barrick's (1977b) model and relies on the relationship between the ocean wind-wave spectra $S_{ww}(f)$ and the normalized, weighted second-order spectra referred to as $R_W(f)$:

$$S_{ww}(f) = \alpha_w \frac{2R_W(f)}{k_o^2}, \tag{22}$$

where α_w is the wind-wave coefficient, which was found to be relatively constant for all wave frequencies (Alattabi et al. 2019), k_o is the radar wavenumber, and $R_W(f)$ is defined by Barrick (1977a,b) as

$$R_W(f_D) = \frac{\sigma_2(f_D)/W(f_D/f_B)}{\sigma_1(f_D) df_D}, \tag{23}$$

where $\sigma_1$and σ_2 are the first- and second-order spectral energies, W is Barrick's weighting function, f_D and f_B are Doppler and Bragg frequencies and df_D is the resolution of the Doppler spectrum. The inverted ocean wave frequency f is determined by $f = |f_D - f_B|$. The weighting function (W) as a function of inverted wave frequencies $f = |f_D - f_B|$ and for two different radar frequencies (12 and 48 MHz) are shown in in Fig. 3. The negative and positive frequencies refer to the weighting function for the inner and outer second-order sidebands, respectively.

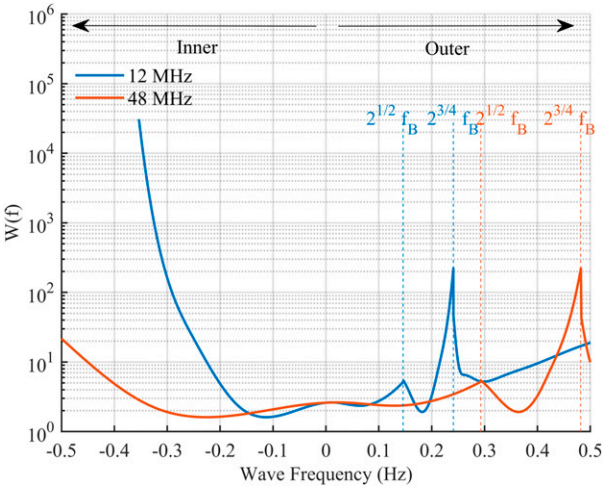

FIG. 3. Barrick's weighting function for 12 and 48 MHz in terms of ocean wave frequency. "Inner" and "Outer" refer to second-order sidebands toward the zero Doppler frequency (i.e., left and right of the Bragg peak for positive and negative Doppler frequencies) and toward $\pm\infty$ Doppler frequency (i.e., right and left of the Bragg peak for positive and negative Doppler frequencies), respectively.

d. Wind and wave direction

The wind direction is estimated using the ratio of Bragg peak energies (Long and Trizna 1973; Stewart and Barnum 1975; Heron and Rose 1986; Fernandez et al. 1997):

$$\zeta = \frac{\sigma_1^+}{\sigma_1^-}, \tag{24}$$

where σ_1^+ and σ_1^- are the integral of first-order spectra (the Bragg peak energies) corresponding to the approaching (+) and receding (−) Bragg waves, respectively. Then, the inverted wind direction is estimated as

$$\theta_w = \theta_r \pm 2\arctan(\zeta^{1/s}), \tag{25}$$

where the ± sign denotes the ambiguity for direction for single radar, which can be resolved using Eq. (16) and two beams from two radar sites pointing at the same location in the ocean. s is the wave directional spreading factor [$s = 2$, as in Gurgel et al. (2006) and Fernandez et al. (1997)].

The direction of wind waves can be estimated from the second-order continuum as in Alattabi et al. (2019) using the ocean-wave-frequency-dependent ratio $\gamma(f)$ of second-order Doppler spectrum energies corresponding to the approaching (positive Doppler frequencies) and receding (negative Doppler frequencies) sides of the second-order sidebands around the dominant Bragg peak ($\sigma_2^{+1,m_2}/\sigma_2^{-1,m_2}$), where $m_2 = \pm 1$ (see Fig. 1). This ratio is defined as

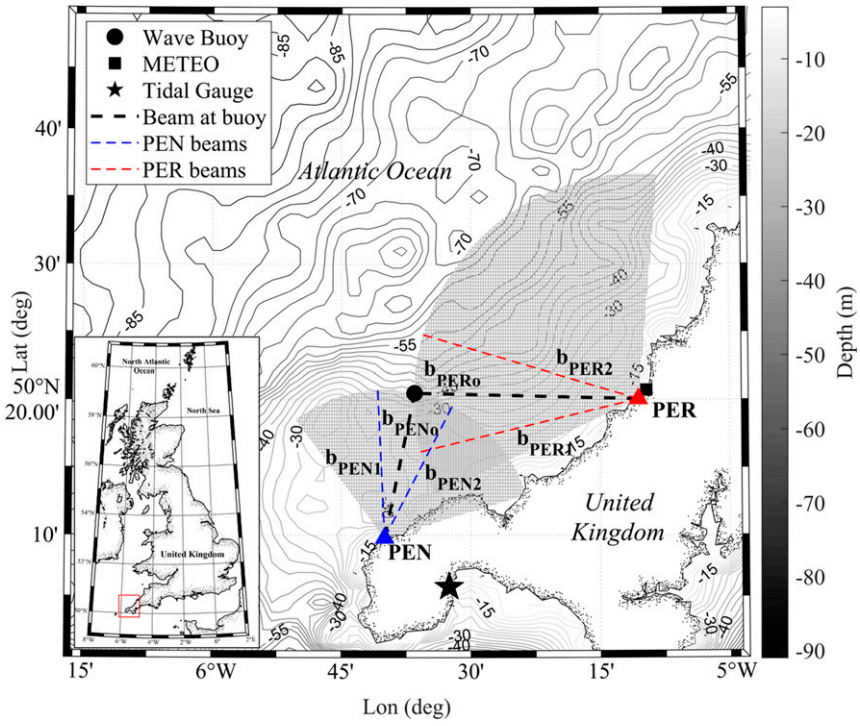

FIG. 4. Map showing the study area in Cornwall and the HF radar installation sites at PEN and PER shown as blue and red triangles, respectively. The locations of the wind and tide gauge stations used in this study are indicated by a square and a star symbol, respectively, while the wave buoy deployment location is shown as a solid black circle. The black dashed lines indicate the radials (beams) used for the inversions (b_{PENo} and b_{PERo} for PEN and PER sites, respectively). The dashed blue and red lines denote the two radials (beams) used for single site inversions and they form a 30° angle (b_{PEN1} and b_{PEN2} for PEN site, and b_{PER1} and b_{PER2} for PER site). Depth contours are shown in meters.

$$\gamma(f) = \frac{\sigma_2^{+1}(f)}{\sigma_2^{-1}(f)}, \tag{26}$$

and the second-order sidebands around the positive and negative Bragg peaks are defined based on the data quality criteria (see section 4) as follows:

$$\sigma_2^i(f) = \begin{cases} \sigma_2^{i,-1}(f) + \sigma_2^{i,+1}(f) & \text{both side continua are available} \\ \sigma_2^{i,-1}(f) & \text{only left-side continuum is available} \\ \sigma_2^{i,+1}(f) & \text{only right-side continuum is available} \end{cases},$$

where $i = +1$ and -1 correspond to second-order sidebands around the positive and negative Bragg peak, respectively. The inverted wave direction is estimated using

$$\theta(f)_{\mathrm{inv}} = \theta_r \pm 2\arctan[\gamma(f)^{1/s}], \tag{27}$$

where $\theta(f)_{\mathrm{inv}}$ is the direction of ocean waves with frequency f, θ_r denotes radial beam direction, and s is the wave directional spreading factor as in Eq. (25). In a similar manner for the case of wind direction, the ambiguity in the solution of Eq. (27) can be resolved using two radar sites with Eq. (16) or auxiliary information.

e. Directional frequency wind-wave spectrum model

The directional wave spectrum $S(f, \theta)$ can be expressed in terms of one-dimensional wave spectrum $S(f)$ and the directional spreading function $D(f, \theta)$ (Longuet-Higgins 1963) as

$$S(f,\theta) = S(f)D(f,\theta), \tag{28}$$

where f is wave frequency and θ is wave direction in radians. Longuet-Higgins (1963), suggested a $\cos^{2s}$ based $D(f, \theta)$ with s being the spreading parameter, which depends on the ratios f/f_p and U_{10}/c_p (Hasselmann et al. 1980). However, this dependence

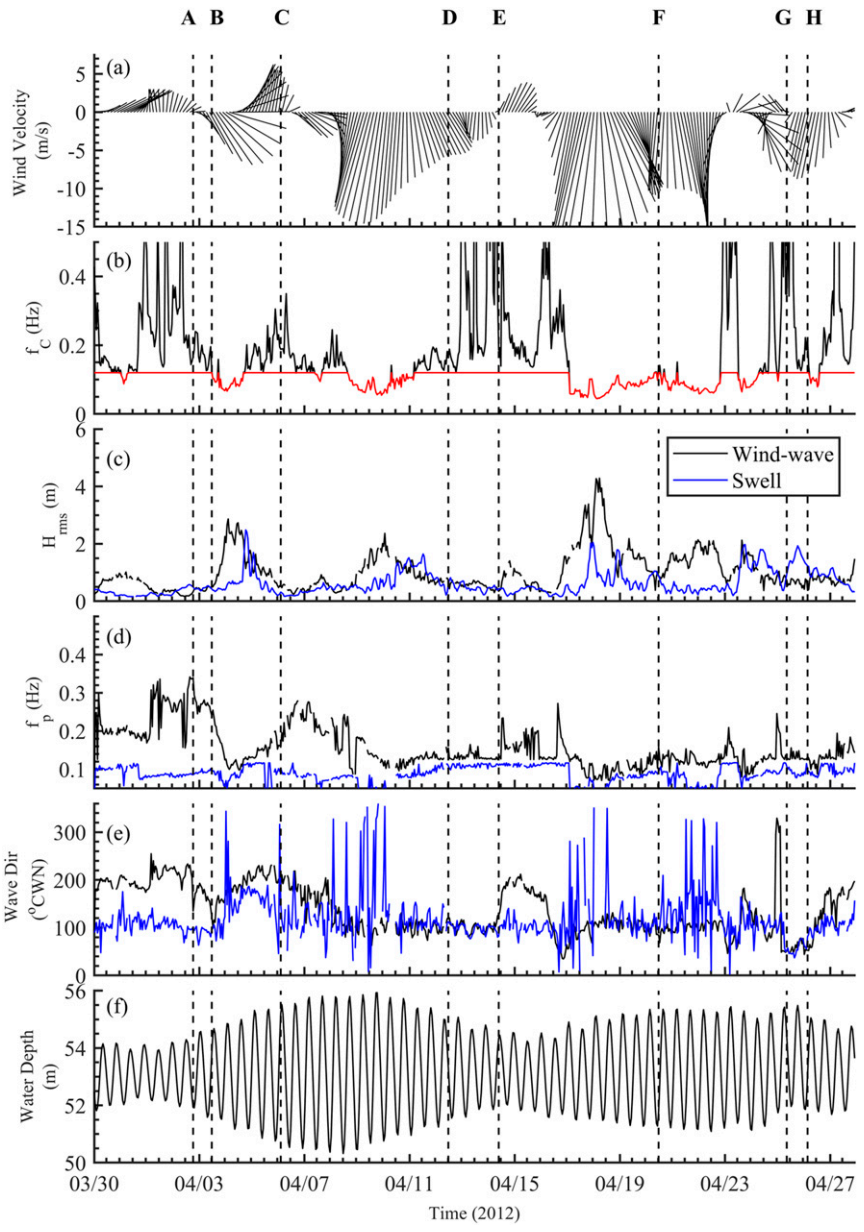

FIG. 5. Time series of wind forcing (measured at the coastline near PER) and partitioned wind-wave (black) and swell (blue) parameters at the wave buoy location (see Fig. 4): (a) wind vector diagram and (b) swell—wind separation frequency. The black line shows the values estimated using Eq. (31), while the red line shows the values adopted after applying the maximum cutoff frequency limit of 0.12 Hz (see text for details), (c) partitioned wind-wave and swell RMS wave heights, (d) partitioned peak frequencies for wind waves and swell, (e) mean direction for wind waves and swell (from true north), and (f) water depth (in m) measured at Newlyn tide gauge station (station ID 202). The vertical dashed lines identify specific wind waves/swell events (A to H) discussed in detail in this study (see text for details).

on wind speed makes the application of the model for HF radar inversion more complicated. Donelan's et al. (1985) directional distribution model is more convenient as it does not depend on wind speed and utilizes a sech^2 function:

$$D(f,\theta) = 0.5\beta \,\mathrm{sech}^2\beta[\theta - \theta(f)], \tag{29}$$

where β depends on the ratio of f/f_p only, so that

$$\beta = \begin{cases} 2.61(f/f_p)^{1.3} & 0.56 < f/f_p < 0.95 \\ 2.28(f/f_p)^{-1.3} & 0.95 < f/f_p < 1.60 \\ 1.24 & f/f_p \geq 1.60 \quad \text{or} \quad f/f_p \leq 0.56 \end{cases}. \tag{30}$$

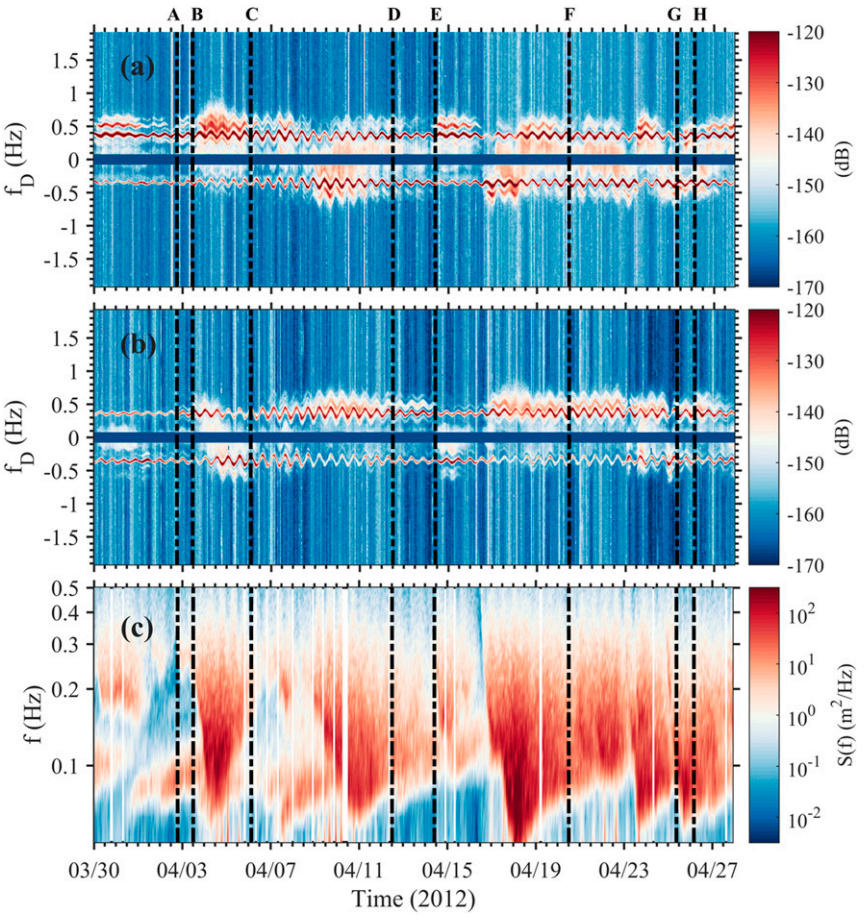

FIG. 6. Time stacks of HF radar Doppler spectra at the wave buoy location from (a) PEN and (b) PER radar systems (b_{PENo} and b_{PERo} beams; see Fig. 4). (c) Time stack of corresponding wave spectral energy density $S(f)$ as estimated using the wave buoy data. Vertical dashed lines A to H identify specific wind waves/swell events.

This distribution is adopted in this study to define the directional characteristics of the inverted wave frequency spectrum.

3. Data availability

Data from two HF radar systems and a wave buoy deployed off the north coast of Cornwall (United Kingdom) are used in this study. Information on wind speed and direction were obtained from a meteorological station located on the coastline at Perranporth (see Fig. 4) while the closest tide gauge (British Oceanographic Data Centre station ID 202) was located on Newlyn. The dataset used in this study covers the period from 30 March to 27 April 2012 and includes simultaneously collected Doppler spectra from the two HF radars and in situ spectral wave data from the buoy. The area is characterized by both swell and wind waves and tidal currents reaching velocities up to 1 m s^{-1} (Pingree 1980).

a. HF radar data

The HF radar data were collected by two 16-element, beamforming HF radar systems Wellen Radar (WERA), deployed on the northern coast of Cornwall (United Kingdom) and operated by the University of Plymouth. The HF radar units were located at Pendeen (PEN) and Perranporth (PER), some 40 km away from each other (Fig. 4) and their boresights were 23° and 305°N, respectively (see Fig. 4). The radars operated at a central transmitting frequency of 12 MHz with a bandwidth of 150 KHz, resulting to a range resolution of 1 km. Data collection was once per hour with a transmission duration of approximately 18 min. A total of 694 transmissions were available for analysis covering the 29-day data collection period used in this study. The Doppler spectra have a frequency resolution of 0.0075 Hz and cover the range −1.915 to 1.922 Hz (defined by the chirp rate of 3.85 Hz used during transmission). The Doppler spectral energy is expressed in decibels (dB) defined using a system internal reference level. Doppler spectra estimations are based on FFT analysis performed on 512-point segments with 75% overlap. For this analysis, Doppler spectra for different beams and sites are utilized depending on the model used for the swell inversion. More details about the HF radar systems and their

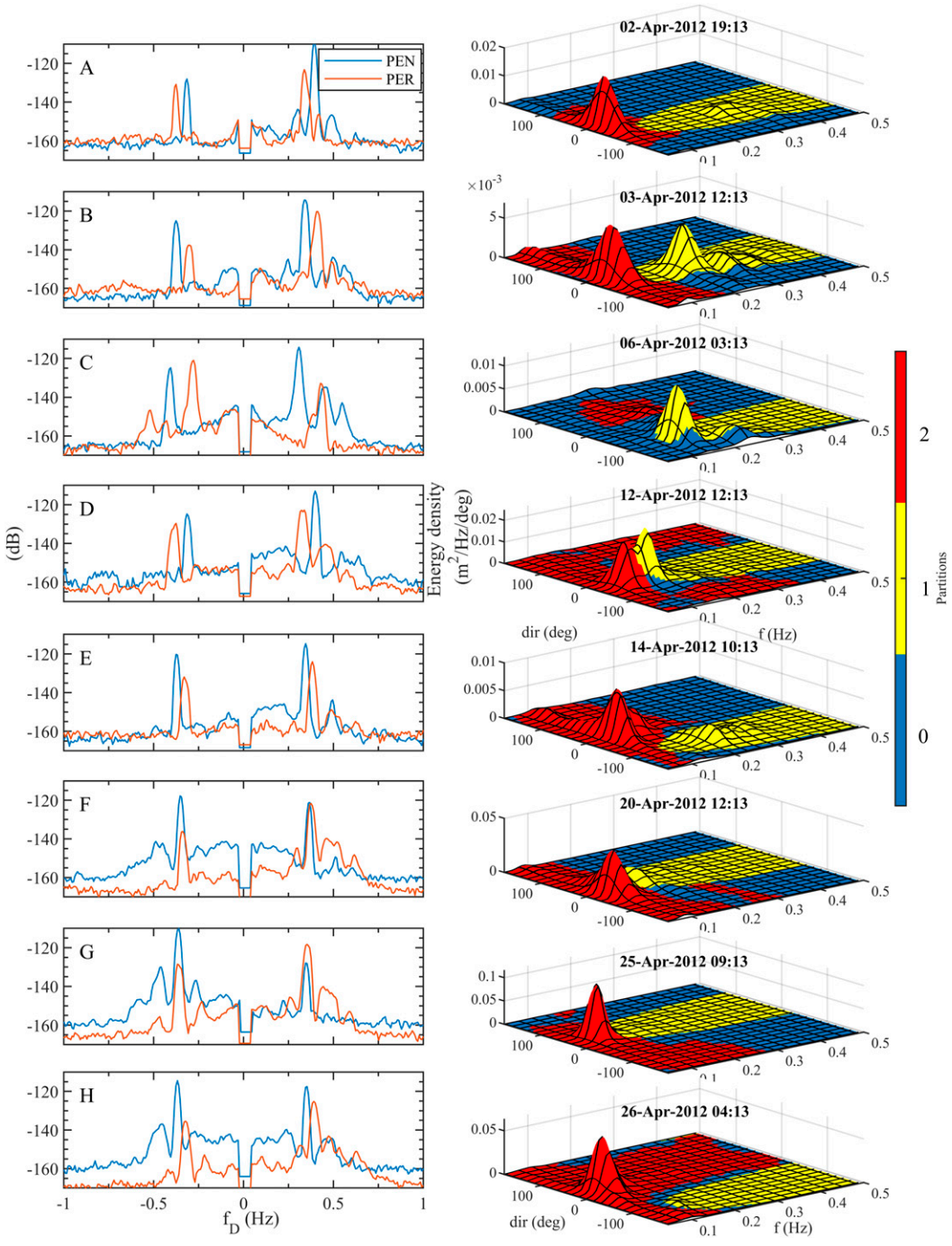

FIG. 7. (left) Individual HF radar Doppler spectra for PEN (blue) and PER (red) sites corresponding to wave events A to H (see Fig. 6). (right) Directional wave spectra for the same events with the swell and wind-wave partitions identified using red and yellow shading. Dark blue corresponds to background noise not associated with surface waves.

configurations can be found in Lopez et al. (2016) and Lopez and Conley (2019).

b. *In situ wave data*

In situ wave data were collected using a Seawatch Mini II directional wave buoy deployed at a mean water depth of 50 m at ranges 20 and 30 km from the PEN and PER HF radar sites, respectively (see Fig. 4). Directional wave spectra estimates were provided every 30 min and the frequency and azimuthal resolution of the spectra are 0.0078 Hz, and 4°, respectively. Although wave spectra cover the frequency range 0.046–0.50 Hz, the analyses were restricted to 0.35 Hz

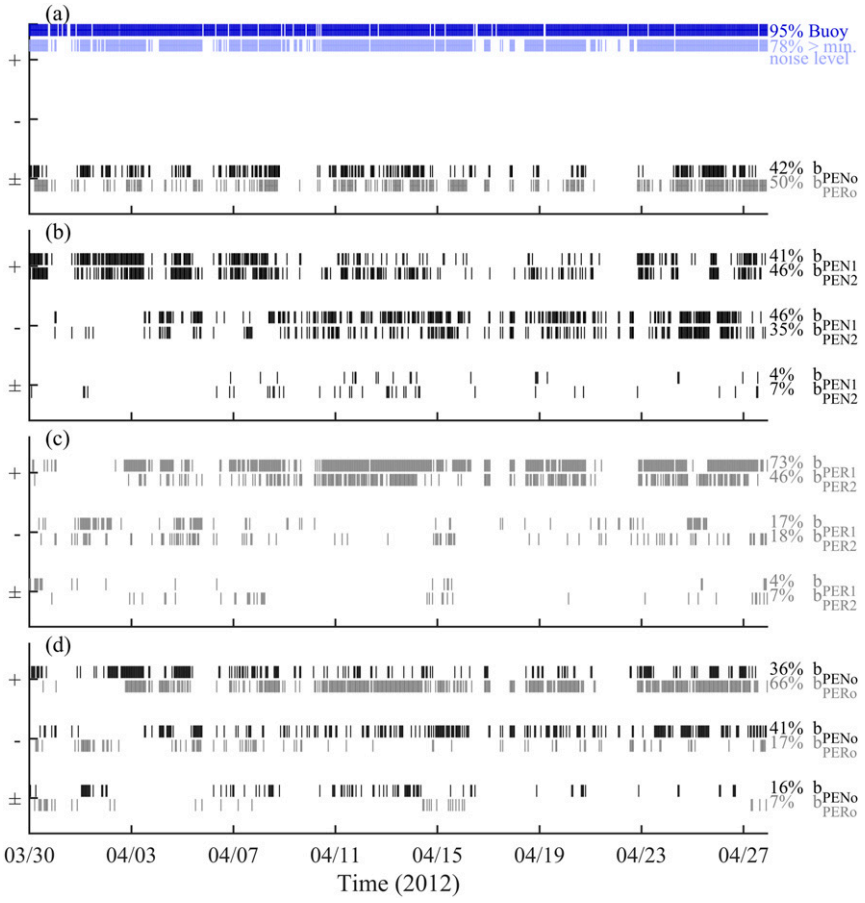

FIG. 8. Instances when swell peaks are identifiable in the Doppler spectra for use in the swell inversion using (a) one beam from a one-site method, (b) two beams from one site (PEN), (c) two beams from one site (PER), and (d) two beams from two sites. Key: ± represents instances where all four swell-induced peaks are identifiable in a single Doppler spectrum; − and + when two peaks are identifiable on the negative and positive side of the Doppler spectra, respectively. The black and gray lines denote the data beams from PEN and PER radar sites, respectively. Note that b_{PENo} and b_{PERo} denote beams from PEN and PER sites pointed at buoy location, b_{PEN1} and b_{PEN2} beams from PEN site, and b_{PER1} and b_{PER2} beams from PER site (see Fig. 4). The dark blue marks in (a) denote swell recorded by the wave buoy while the light blue marks denote instances when the recorded swell was above the minimum noise level ($0.15\,m^2\,Hz^{-1}$) required for evaluating the swell inversion algorithms. Their percentages are estimated over the total data available. The percentage of radar data availability is shown for each case and represent data availability over the number of in situ swell data points that passed the minimum noise level criterion.

as this corresponds to the maximum ocean wave frequency resolved by the HF-radar-derived Doppler spectra.

RMS wave height and peak and mean wave frequencies and directions were estimated from the directional spectra using the moments method (Herbers et al. 1999). Swell and wind-wave bulk wave parameters were estimated by partitioning the spectra using a watershed defining algorithm as implemented by Cahl and Voulgaris (2019).

4. Methodology

Prior to analysis, the noise level of the Doppler spectrum is estimated using the method described in Hildebrand and Sekhon (1974) and then subtracted from the spectra. The energy levels for the first- and second-order regions of the denoised Doppler spectra (σ_1 and σ_2, respectively) are used to check spectra suitability for inversion and to avoid cases where the first and second-order spectra are merged. The values of the above data quality control criteria (i.e., $\sigma_1 > 25$ dB and $\sigma_2 > 10$ dB) suggested by Alattabi et al. (2019), although suitable for the 48 MHz VHF radar used in their study, were found to be very restrictive in this case (12 MHz) qualifying only for a small percentage of the data (~20%) for inversion. This is mainly due to differences in power emission, and attenuation levels due to differences in operating frequencies and ranges (48 MHz at 4 km and 12 MHz at 20–30 km). After visual

TABLE 1. List of statistical parameters from the comparison of in situ swell frequency with estimations from LPM and EMP (see Fig. 9). NRMS error is the RMS error normalized by frequency resolution; r is the correlation coefficient; slope is the regression slope; and N and % represent the number and percentage of records used in the comparison. The term "Common" denotes cases when both stations had spectra suitable for inversion, while the term "Combined" denotes instances when spectra were suitable from one or both stations (see text for details).

No. of sites and beams used	Model	Site	Beam 1 (°N)	Beam 2 (°N)	N	%	RMS error (Hz)	NRMS error (RMS/df)	r	Slope
One site–one beam	LPM1, Eq. (3)	PEN	13	—	263	48	0.0152	1.94	0.40	0.92
		PER	272	—	324	60	0.0141	1.81	0.59	0.90
		Common	—	—	164	30	0.0111	1.42	0.60	0.92
		Combined	—	—	423	78	0.0147	1.88	0.50	0.90
One site–two beams	$LPM2_1$, Eqs. (8) and (9)	PEN	28	355	400	74	0.0144	1.84	0.31	0.95
		PER	287	256	375	69	0.0117	1.50	0.60	1.07
		Common	—	—	270	50	0.0083	1.06	0.60	1.03
		Combined	—	—	505	93	0.0123	1.57	0.42	1.00
	$EPM2_1$, Eq. (21)	PEN	28	355	269	49	0.0099	1.27	0.55	0.95
		PER	287	256	394	72	0.0108	1.38	0.62	0.93
		Common	—	—	222	41	0.0095	1.21	0.60	0.94
		Combined	—	—	441	81	0.0098	1.25	0.66	0.93
Two sites–two beams	$LPM2_2$, Eqs. (8) and (9)	PEN and PER	13	272	366	67	0.0130	1.67	0.60	0.97
	$EPM2_2$, Eq. (21)	PEN and PER			280	51	0.0112	1.43	0.61	0.94

examination of the Doppler spectra, it was concluded that the best quality criteria were (i) first-order Bragg peaks and second-order sideband energy levels (σ_1 and σ_2) greater than 10 and 5 dB, respectively, and (ii) the energy of the Bragg peak should be at least 2 dB higher than the mean energy of the 1/3 highest second-order peaks present in the Doppler spectrum.

The inverted spectral frequencies are limited by the lower-frequency limit of the second-order sidebands that for this dataset corresponds to a lower wave frequency ($f_{\min}$) of 0.046 Hz (Doppler frequency = ± Brag frequency ± 0.046 Hz); frequencies lower than that value are often contaminated by energy from the first-order signal. The upper limit of the Doppler spectra is limited to a maximum ocean wave frequency of 0.35 Hz, which corresponds roughly to the distance (in Hz) of the first-order Bragg peak from the zero Doppler frequency. Although some studies utilizing a 12-MHz system have used the range 0.05–0.25 Hz with a resolution of 0.01 Hz (e.g., Wyatt 2005, 2017; Lopez et al. 2016; Lopez and Conley 2019), Gurgel et al. (2006) has argued that the upper limit can be safely extended up to 0.35 Hz as done in this study.

The swell region is defined as the area around the dominant Bragg peak that corresponds to ocean wave frequency range $f_{\min}$ to f_c, where f_c is the swell—wind separation frequency. The latter is determined using the wave age formulation (Hanson and Phillips 2001) that relates wind speed to peak wind-wave frequency:

$$f_c = \frac{g}{2\pi}\left(\frac{1}{TU_{10}}\right), \tag{31}$$

where T is an empirical factor and U_{10} is the wind speed at 10 m above sea level. Although T has been found to range from 1.25 to 1.9 (Gilhousen and Hervey 2002; Hanson and Phillips 2001; Chen et al. 2015; Hessner and Hanson 2010; Bidlot 2001; Tracy et al. 2007; De Farias et al. 2012; Churchill et al. 2006; Earle 1984; Quentin 2002); $T = 1.5$ is adopted here as it is the most commonly used value (Hanson and Phillips 2001; Chen et al. 2015; Hessner and Hanson 2010). In addition, the maximum swell separation frequency obtained using Eq. (31) is not allowed to exceed 0.12 Hz.

Once the swell region has been defined, the peak swell Doppler frequency f_{Dj} is estimated using the weighted mean of the largest peak identified (f_{Dm}) within this region and two points on either side of it:

$$f_{Dj} = \frac{\sum_{i=-2:2} \sigma_2 (f_{Dm+i})^n f_{Dm+i}}{\sum_{i=-2:2} \sigma_2 (f_{Dm+i})^n} \quad f_{\min} < f_{Dm+i} < f_{Dc}, \tag{32}$$

where f_{Dm+i} is the discrete Doppler frequency where a Doppler estimate is available and f_{Dc} is the swell–wind separation frequency expressed as Doppler frequency (i.e., $f_c = |f_{Dc} - f_B|$). The value of $n = 5$ was selected in (32) as this has been found to reduce the errors associated with peak estimations from discrete frequency spectra (Young and Verhagen 1996). The measured swell peak ratio R_j is then defined as

$$R_j = \frac{\int_{f_{Dm-2}}^{f_{Dm+2}} \sigma_2(f_D)\, df_D}{\int_{f_B-\Delta f}^{f_B+\Delta f} \sigma_1(f_D)\, df_D}, \tag{33}$$

where df_D is the resolution of the Doppler spectrum. For Bragg peaks, Δf is defined as the half-power frequency width of Bragg peaks obtained after fitting a Gaussian curve around

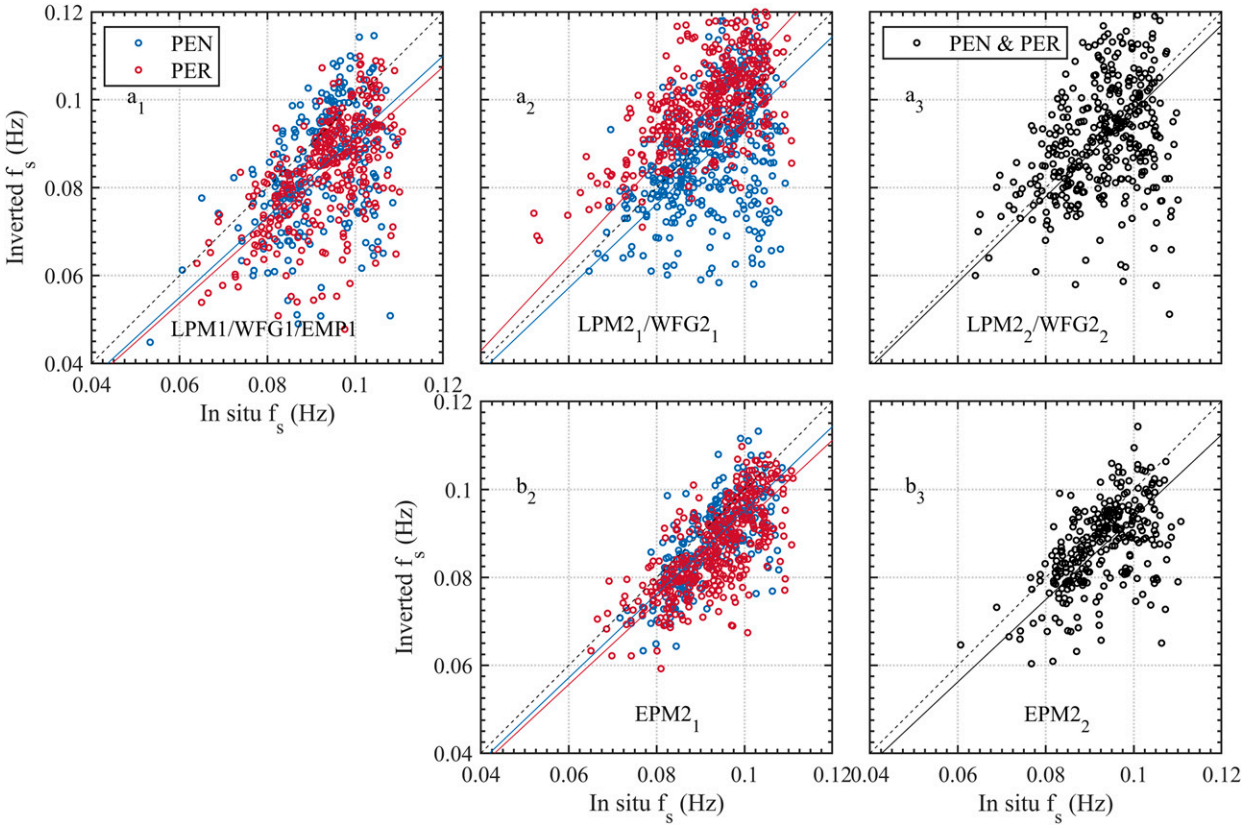

FIG. 9. Scatterplot of inverted and in situ swell frequencies using (a_1) one beam from a single site (LPM1, WFG1, and EPM1); (a_2) two beams from a single site (LPM2$_1$ and WFG2$_1$); (a_3) two beams from sites PEN and PER, respectively (LPM2$_2$ and WFG2$_2$); (b_2) two beans from a single site (EPM21); and (b_3) as in (a_3), but using the EPM2$_2$ method. For statistics, see Table 1.

the Bragg peak using two points of either side of it (Alattabi et al. 2019; Wang et al. 2014).

For one site/one beam analysis, the swell models LPM1, WFG1, and EMP1 are utilized using the radar radial data (b_{PENo} and b_{PERo}) pointing directly to the buoy location (see dashed black lines in Fig. 4). The same radial beams (b_{PENo} and b_{PERo}) are used when the two sites–two beams methods (i.e., LPM2$_2$, WFG2$_2$, and EMP2$_2$) are utilized. For one site–two beams analysis (i.e., LPM2$_1$, WFG2$_1$, and EMP2$_1$) data from two radial beams from a single radar site (b_{PEN1} and b_{PEN2} for PEN site; b_{PER1} and b_{PER2} for PER site), directed 15° on either side of the buoy location are used. These are schematically shown as red and blue dashed lines in Fig. 4, for PEN and PER sites, respectively.

5. Results

a. Wave and wind conditions

The recorded in situ wind and wave conditions for the period from 30 March to 17 April 2012 used in this study are shown as time series in Fig. 5. The total RMS wave height ranged from 0.23 to 5.0 m while peak wave frequency ranged from 0.034 to 0.30 Hz. The partitioned wind-wave and swell parameters are shown in Figs. 5b–e. The swells present travel across the North Atlantic either from the west or southwest and their RMS wave heights ranged from 0.1 to 2.1 m (see Figs. 5b,e).

During the experimental period several wind-wave and swell events are identified, but for model verification, only events with qualifying (i.e., $\sigma_1 > 10$ dB and $\sigma_2 > 5$ dB and $\sigma_1/\sigma_2 > 2$) Doppler spectra are analyzed. Specific events (A–H) are identified that correspond to periods when only swell (A, G, and H), only wind waves (C), mixed (swell and wind wave) conditions with similar energy in both wave bands (B and D), and mixed waves with swell being the dominant band (E and F). During event A light swell waves with height ~0.5 m propagating mostly from the west (mean swell direction ~95°N) is present. While event B presents both wind wave with height ~0.5 m and swell wave with height ~0.37 m, where swell is propagating from the same direction of event A. Events G and H represent strong swell activity (swell height up to 1.3 m) with mean directions 53° and 81°N, respectively. Overall, the swell during events A and B cross the PEN radar beam at the buoy location at high (>80°) cross angles, while the cross angles for events G and B are smaller (41° and 69°, respectively). The same swell trains cross the PER beam at very small angles of 2° and 5° for events A and B, respectively. A moderate cross angle (38°) was recorded for PER site at event G.

b. HF radar Doppler and in situ wave spectra

Time stacks of Doppler spectra corresponding to the buoy location and for the whole period of data availability are shown

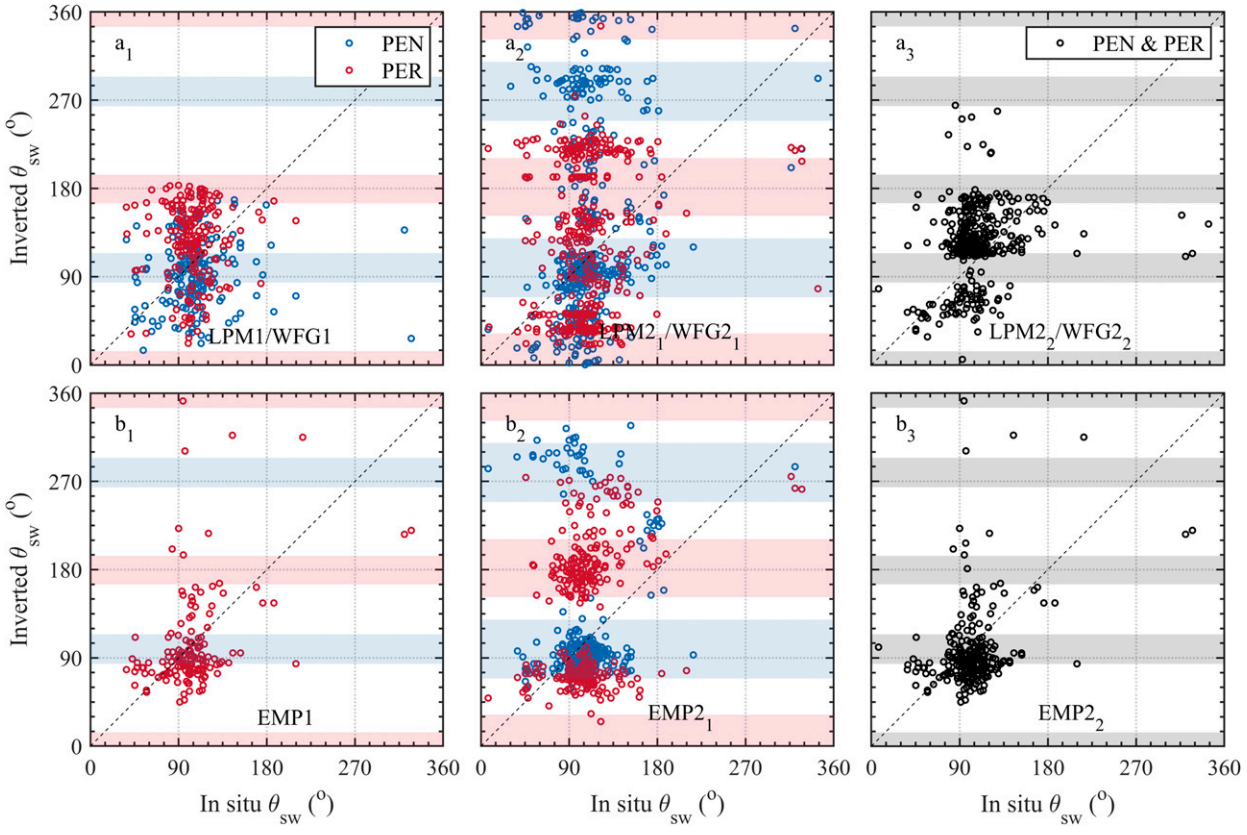

FIG. 10. Scatterplot of inverted and in situ swell directions using the (a_1)–(a_3) LPM and (b_1)–(b_3) EMP methods, for PEN (blue circles) and PER (red circles). The methods utilized used one site–one beam in (a_1) and (b_1), one site–two beams in (a_2) and (b_2), and two sites–two beams in (a_3) and (b_3). The shaded ranges denote the range of inverted swell cross angle $|\theta_s| > 75°$ that are excluded from swell wave height inversions. For statistics, see Table 2.

in Figs. 6a and 6b for both radar sites. The Doppler Bragg (first-order) peaks are modulated by the tidally induced surface currents while the energy of the second-order continuum is visible around the first-order peaks. It is worth noting that the second-order regions are significantly narrower for PER (Fig. 6b) than for PEN (Fig. 6a). Similarly, a time stack of the in situ wave spectra is shown in Fig. 6c. The specific swell and wind-wave events (A–H) are also identified in the figure while the detailed wave directional spectra for each individual event are shown against the corresponding Doppler spectra in Fig. 7. In the same figure, the partitioned regions of the spectra derived using the method of Cahl and Voulgaris (2019) are shown using red and yellow shading for swell and wind waves, respectively.

c. *Swell wave inversion*

In this section, the results for the swell inversion are presented and include inversions using: 1) a single beam from a single radar site ($LPM1_1$, $WFG1_1$, $EMP1_1$), 2) two beams from a single radar site ($LPM2_1$, $WFG2_1$, $EMP2_1$), and 3) two beams from two sites (a single beam per site) intersecting each other at the buoy location ($LPM2_2$, $WFG2_2$, $EMP2_2$). Only Doppler spectra that passed the data quality control (see section 4) are used for the inversion. Data that passed the data quality control but in which no swell peaks were present were also excluded from the analysis. The lack of swell peaks can be attributed to no swell being present in the ocean or not being detected in the Doppler spectrum. Analysis of the buoy data revealed that swell was present 95% of the time (658 data points), but swell with energy density above a minimum energy level defined as $0.15\,m^2\,Hz^{-1}$ represents 78% of the total (i.e., 544 data points). The times where the Doppler spectra passed the quality criteria and swell peaks were identified are shown in Fig. 8 together with in situ swell percentage of data availability and in situ swell data with energy level above $0.15\,m^2\,Hz^{-1}$. The labels on the *y*-axis scale denote the side of Doppler spectrum that swell peaks are identified [i.e., (−) and (+) denote the negative and positive sides of the Doppler spectrum, respectively, while (±) denotes both sides (i.e., four peaks)].

1) INVERSION FOR SWELL FREQUENCY

(i) Single site

A. ONE SITE–ONE BEAM

Inversion for swell frequency with this method requires that within a single Doppler spectrum four swell peaks are detected; this requirement is identical for all three swell inversion models ($LPM1_1$, $WFG1_1$, $EMP1_1$) [see Eq. (3) and Table 1]. Doppler

TABLE 2. Evaluation of the different swell direction inversion methods (see text for details and Fig. 10) against in situ data. The parameters listed are RMS error (RMSE), magnitude ($|r|$) and angle (in degrees) of complex correlation coefficient (r), and number (N) and the corresponding percentage of data points used for the comparison. The terms "Common" and "Combined" are as described in Table 1 (see text for details).

No. of sites and beams used	Model	Site	Beam 1 (°N)	Beam 2 (°N)	N	%	RMS error (°)	Complex r	
								$\|r\|$	Angle (°)
One site–one beam	LPM1, Eq. (2)	PEN	13	—	116	21	59	0.18	40
		PER	272	—	155	28	54	0.06	−46
		Common	—	—	50	9	40	0.09	4
		Combined	—	—	221	41	54	0.09	6
	EMP1, Eq. (16)	PEN	13	—	101	19	57	0.34	−13
		PER	272	—	146	27	44	0.31	4
		Common	—	—	99	18	51	0.37	−8
		Combined	—	—	148	27	49	0.39	−1
One site–two beams	$LPM2_1$, Eqs. (8)–(11)	PEN	28	355	176	32	86	0.39	19
		PER	287	256	135	25	57	0.20	6
		Common	—	—	44	8	73	0.40	37
		Combined	—	—	267	49	99	0.33	16
	$EMP2_1$, Eq. (16)	PEN	28	355	46	8	85	0.52	−27
		PER	287	256	212	39	71	0.03	1
		Common	—	—	11	2	68	0.57	4
		Combined	—	—	247	45	73	0.10	−12
Two sites–two beams	$LPM2_2$, Eqs. (8)–(11)	PEN and PER	13	272	267	49	48	0.53	20
	$EMP2_2$, Eq. (16)	PEN and PER			148	27	46	0.37	−7

spectra from beams b_{PERo} and b_{PENo} are used here and the inversion is carried out on those Doppler spectra that passed the quality assurance (QA) criteria where swell peaks were successfully identified. These represent 48% and 60% of the record with swell detected in the in situ data for PEN and PER, respectively.

Higher data availability (78%) is obtained when we count the times that spectra from one or both sites passed the criteria for successful inversion for swell frequency (see Table 1, "combined"). The inverted swell frequencies are compared to the in situ data in the scatterplot shown in Fig. $9a_1$ and the statistics of the comparison are listed in Table 1. The correlation coefficients are 0.40 and 0.59 for PEN and PER, respectively while the RMS error is just above 0.01 Hz but always less than 2 times the frequency resolution. Using the inversions from the periods when data from both stations ("common" in Table 1) were usable (30% of the data,) the correlation coefficient was similar to that for PER.

B. ONE SITE–TWO BEAMS

When two beams from a single site (b_{PEN1} and b_{PEN2} from PEN and b_{PER1} and b_{PEN2} from PER, see Fig. 4) are used, the two swell peaks identified on the dominant side of each beam's Doppler spectra are utilized [see Eqs. (8) and (9) for both $LPM2_1$ and $WFG2_1$, and Eq. (21) for $EPM2_1$]; these could be on either positive or negative sides of the spectra. The Doppler spectra that passed the QA criteria and swell peaks were successfully identified were 74% and 69% of the record with swell present for PEN and PER, respectively. Combining the records from both sites increases the percentage to 93%. The times both stations had spectra suitable for inversion (common) represent only 50% of the swell record.

The results of this inversion are compared with the in situ derived swell frequencies in the scatterplot shown in Figs. $9a_2$ and $9b_2$ for $LPM2_1$/$WFG2_1$ and $EPM2_1$, respectively. The statistics of the comparison (Table 1) indicate that although the RMS error for the $LPM2_1$/$WFG2_1$ method is the same (just above 0.01 Hz) the estimations using spectra from PER exhibit less variability ($r = 0.60$) than those from PEN ($r = 0.31$). $EPM2_1$ [see Eq. (21)] estimates show similar variability for both radar sites ($r \sim 0.62$). As expected, the variability of the common and combined inversions, as expressed though the value of the correlation coefficient varies as a function of the number of points used from each site and the r values of the individual sites ($r = 0.31$ and 0.60 for PEN and PER, respectively).

(ii) Two sites

When two sites are used, the same Eqs. (8), (9), and (21), as before, are utilized for $LPM2_2$ and $EMP2_2$, respectively. The only difference is that the beams b_{PERo} and b_{PENo} aiming directly at the in situ buoy are used (see Fig. 4) in this case. The Doppler spectra available for this method represent 67% and 51% of the record with swell present for $LPM2_2$ and $EMP2_2$, respectively. The comparison of the inverted and in situ swell frequency values is shown in Fig. $9a_3$ in the form of a scatterplot and in Table 1. The swell frequency inversions using these methods show a relatively higher correlation coefficient (>0.60) than those derived using the one site-one beam, and one site-two beam methods (see previous section). These findings are consistent for both $LPM2_2$ and $EPM2_2$ methods (see Figs. $9a_3$,b_3). It should be noted that the WFG method uses the same equations as the LPM method to estimate the

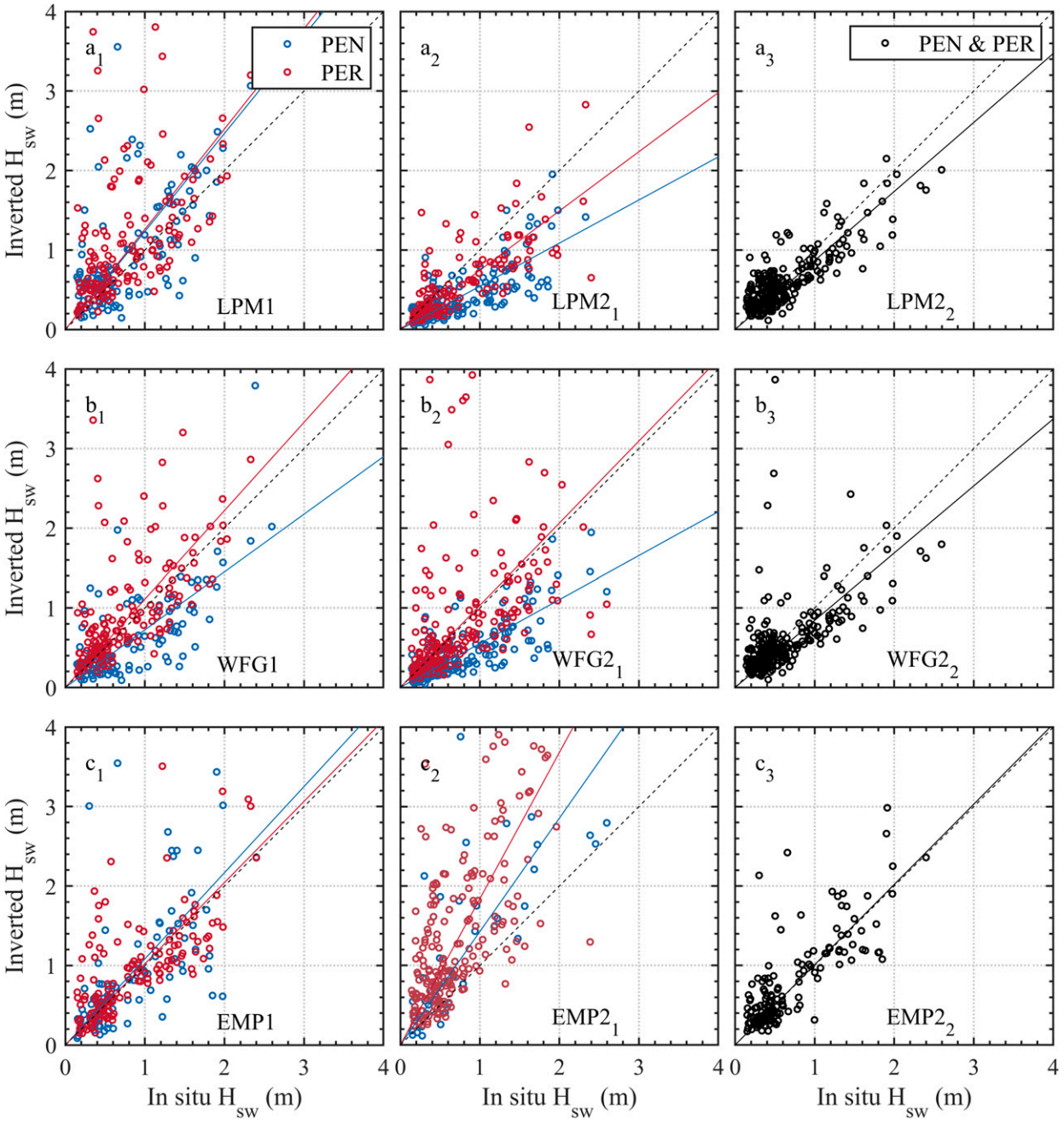

FIG. 11. Scatterplot of in situ and inverted RMS swell wave heights using (a_1)–(a_3) LPM, (b_1)–(b_3) WFG, and (c_1)–(c_3) EMP for PEN (blue circles) and PER (red circles) for (left) one site–one beam, (center) one site–two beam, and (right) two sites–two beams. For statistics, see Table 3.

frequency of the swell, so the results are identical and not shown here.

2) INVERSION FOR SWELL DIRECTION

(i) Single site

A. ONE SITE–ONE BEAM

When four swell peaks are detectable in an individual Doppler spectrum from a single beam, the direction of the swell is obtained using Eq. (2) (LPM1/WFG1 methods) or Eq. (16) (EMP1 method). The direction values derived using these methods are plotted against the swell directions from the buoy data obtained after partitioning the directional spectra (see Figs. 10a_1,b_1). The corresponding statistics are listed in Table 2. It is worth noting that only a very limited fraction of the record with swell present (21%–28%) allowed for the detection of four swell peaks. Even when the data from two sites are combined, the

TABLE 3. Evaluation of the different swell wave height inversion methods (see text for details and Fig. 11) against in situ data. The parameters listed are RMS error (in m), correlation coefficient (r), regression slope, normalized RMS error (NRMS), scatter index (SI), corrected indicator (HH), and bias (BI). The number (N) and percentage (%) of data points used are also shown. The terms "Common" and "Combined" are as described in Table 1 (see text for details).

No of sites and beams used	Model	Site	Beam 1 (°N)	Beam 2 (°N)	N	%	RMS error (m)	r	Slope	NRMS error	SI	HH	BI
One site–one beam	LPM1, Eq. (6)	PEN	13	—	116	21	0.94	0.53	1.23	0.97	0.92	0.97	0.28
		PER	271	—	154	28	0.75	0.53	1.26	0.82	0.73	0.73	0.33
		Common	—	—	50	9	0.60	0.63	1.20	0.58	0.50	0.53	0.31
		Combined	—	—	220	40	0.80	0.56	1.26	0.87	0.80	0.77	0.31
	WFG1, Eq. (13)	PEN	13	—	116	21	0.63	0.51	0.72	0.64	0.62	0.75	−0.17
		PER	272	—	154	28	0.55	0.62	1.11	0.60	0.57	0.57	0.17
		Common	—	—	50	9	0.38	0.72	0.88	0.36	0.36	0.39	−0.03
		Combined	—	—	220	40	0.55	0.57	0.95	0.61	0.60	0.62	0.04
	EMP1, Eq. (18)	PEN	13	—	99	18	0.66	0.64	1.08	0.67	0.66	0.64	0.10
		PER	272	—	144	26	0.47	0.70	1.02	0.47	0.46	0.46	0.10
		Common	—	—	97	18	0.42	0.77	1.05	0.42	0.40	0.41	0.11
		Combined	—	—	146	27	0.40	0.79	1.04	0.40	0.39	0.39	0.09
One site–two beams	$LPM2_1$, Eqs. (10) and (11)	PEN	28	355	170	31	0.45	0.77	0.54	0.52	0.38	0.70	−0.31
		PER	287	256	130	24	0.41	0.73	0.75	0.43	0.40	0.50	−0.15
		Common	—	—	42	8	0.43	0.82	0.67	0.41	0.30	0.51	−0.29
		Combined	—	—	258	47	0.41	0.77	0.63	0.46	0.38	0.58	−0.23
	$WFG2_1$, Eq. (14)	PEN	28	355	194	36	0.44	0.78	0.55	0.51	0.39	0.69	−0.29
		PER	287	256	199	37	0.87	0.43	1.03	0.91	0.90	0.90	0.15
		Common	—	—	75	14	0.52	0.57	0.70	0.53	0.51	0.64	−0.14
		Combined	—	—	318	58	0.66	0.50	0.85	0.74	0.74	0.80	−0.05
	$EMP2_1$, Eqs. (19) and (20)	PEN	28	355	45	8	0.83	0.78	1.43	0.79	0.66	0.66	0.45
		PER	287	256	210	39	1.14	0.57	1.84	1.38	1.07	1.06	0.72
		Common	—	—	11	2	0.41	0.86	1.06	0.40	0.33	0.39	0.23
		Combined	—	—	244	45	1.10	0.61	1.77	1.28	0.99	0.96	0.70
Two sites–two beams	$LPM2_2$, Eqs. (10) and (11)	PEN and PER	13	272	253	47	0.24	0.85	0.87	0.32	0.32	0.34	−0.02
	$WFG2_2$, Eq. (14)	PEN and PER			258	47	0.39	0.62	0.84	0.52	0.52	0.56	−0.02
	$EMP2_2$, Eqs. (19) and (20)	PEN and PER			145	27	0.37	0.79	1.04	0.42	0.42	0.42	0.08

number of inversions represents only 41% of the total record.

B. ONE SITE–TWO BEAMS

When two beams from a single site are used [Eqs. (8)–(11) for $LPM2_1$/$WFG2_1$ and Eq. (16) for $EMP2_1$] the inversion results show significant scatter (see Figs. 10a_2,b_2, and Table 2). The percentage of inverted data from $LPM2_1$ is 25% and 32% for the PER and PEN sites, respectively. A similar percentage is obtained when $EMP2_1$ is used on PER, but the rate of inverted data falls to 8% for the PEN site. When data from both sites are combined the amount of inverted data increases to 45%.

(ii) Two sites

The same equations used in the previous scenario are used in both $LPM2_2$/$WFG2_2$ and $EMP2_2$ methods that utilize two beams from two different sites. The results are shown in Figs. 10a_3 and 10b_3. It seems both methods provide fair estimates of swell direction in this case. The $LPM2_2$ method shows good agreement with the in situ data that is better than that identified when using $LPM2_1$ with a complex correlation coefficient with magnitude of ~0.53 and angle of 20° (see Table 2). The $EMP2_2$ method shows a lower correlation (r = 0.37) than the $LPM2_2$ method.

The WFG method for swell direction is the same as that for the LPM method and as such the same statistics are valid. The statistical results shown in Table 2 are obtained without considering the flagged data (shaded range in Fig. 10) because the latter do not have corresponding inverted swell wave heights. The latter is required to determine the complex correlation coefficient so only data with inverted swell cross angles < 75° [see section 5c(3) below] are used.

3) INVERSION FOR SWELL WAVE HEIGHT

As discussed in section 2 and described in Lipa et al. (1981), singularities at high swell cross angles (~90°, see Fig. 2) do not allow the inversion for swell. A synthetic data analysis (not shown here) using different radar frequencies (4, 12, and 48 MHz), and swell periods varying from 8 to 25 s, revealed that the range of swell cross angles that leads to singularities in the

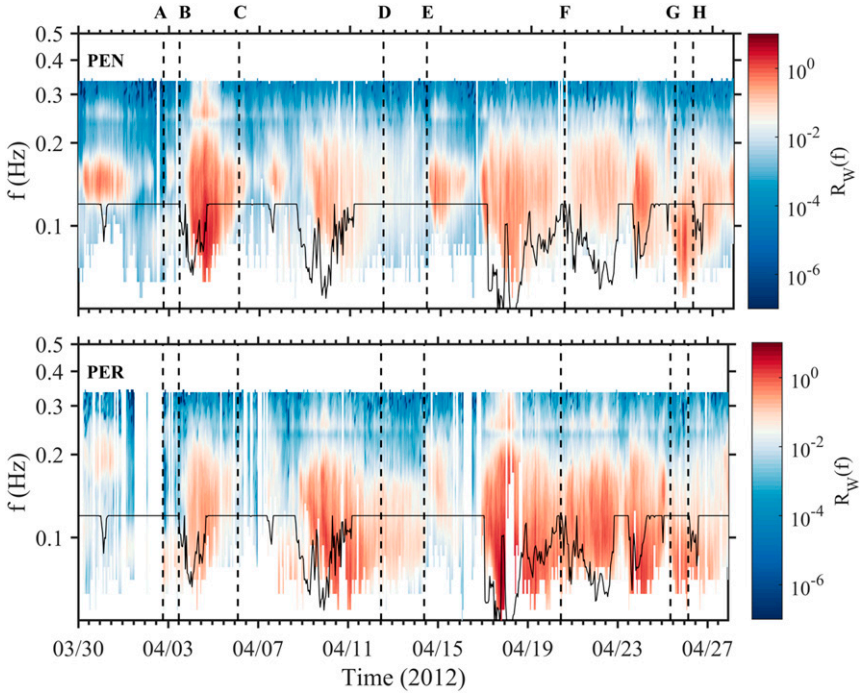

FIG. 12. Time stacks of weighted normalized second-order radar spectra $R_W(f)$ for (top) PEN and (bottom) PER estimated using Doppler spectra from the range and azimuth corresponding to the buoy location [see Eq. (23)]. The solid black curve denotes the separation frequency used in this study (see text for details). Vertical dashed lines marked A–H identify specific wind waves/swell events (see Figs. 6a,b).

coupling coefficient depends on radar operating frequency. For radar frequencies of 4, 12, and 48 MHz singularities occur for swell cross angles $|\theta_s| > 60°$, 75°, and 85°, respectively. A crude, empirical fitting suggests that singularities would occur when $|\theta_s| > 23 \log_{10}(f_{\text{radar}}) + 48$, where f_{radar} is the radar operating frequency (in MHz). In this manuscript, inverted swell cross angle $|\theta_s|$ above the value of 75° are flagged (see previous section, shaded areas in Fig. 10) and not used for swell wave height inversion.

Inverted RMS swell wave heights estimates using all three methods (LPM, WFG, and EMP) and for the different combinations of sites and beams, as described in sections 2a and 2b, are examined in the following sections. The cross-angle limitation leads to swell height inversions from a smaller number of records than those reported for swell direction inversion.

(i) Single site

A. ONE SITE–ONE BEAM

Inverted swell wave height using the LPM1 [Eq. (6)], WFG1 [Eq. (13)], and EMP1 [Eq. (18)] methods are shown in Figs. 11a$_1$–c$_1$, respectively. The percentages of successful inversions were very low (21%, for LPM1 and WFG1 and 18% for EMP1) for PEN and the errors in swell height were 0.94, 0.63, and 0.66 m, respectively. The low rate of inverted data is due to the lack of detectable swell peaks in the swell region of the Doppler spectra. Some of these cases represent weak in situ swell signals (i.e., energy $< 0.76\,\text{m}^2\,\text{Hz}^{-1}$ that corresponds to RMS swell wave height of 0.21 m) that is not detectable by the radar. Similar low recoveries were experienced in applying the inversion Doppler spectra from PER (28%) with the errors being of similar value as those for PEN (see Table 3). The errors are significantly smaller (0.60, 0.38, and 0.42 m, respectively) when averaging the estimates from both stations

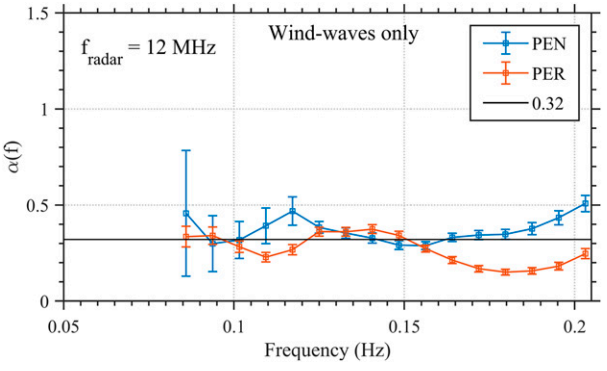

FIG. 13. Wind-wave coefficient $\alpha(f)$ values determined from weighted normalized second-order spectra from PEN (blue) and PER (red) beam data pointing at buoy location using the method described in Alattabi et al. (2019). The solid horizontal line is the averaged $a_w = \alpha(f) = 0.32$ over the frequency range 0.085–0.2 Hz.

(see "common" in Table 3) but in this case the inversion is limited to only 9%–18% of the record.

B. ONE SITE–TWO BEAMS

The comparisons of inverted and in situ swell heights for all three methods that use two beams from a single site ($LPM2_1$, $WFG2_1$ and $EMP2_1$) are presented as scatterplots in Figs. $11a_2$–$11c_2$ and the statistics are listed in Table 3. The results clearly indicate that $EMP2_1$ provides the least favorable agreement (RMS error > 0.80 m) as there is a large scatter between inverted and in situ values (see Fig. $11c_2$). In addition, it appears to overestimate swell heights (regression line slopes > 1, see Fig. $11c_2$ and Table 3). The other two methods ($LPM2_1$ and $WFG2_1$) perform slightly better in terms of RMS errors, although the slope of the regression line suggests underestimation of wave heights; $WFG2_1$ seems to perform best for data from PEN (see Fig. $11b_2$), while LPM21 appears to perform better for data from PER (see Fig. $11a_2$).

(ii) Two sites

Using two beams from two different sites (i.e., methods $LPM2_2$, $WFG2_2$, and $EMP2_2$) seems to provide better agreement with the in situ data (see Table 3) than those shown in the previous section (two beams from a single site). This is the case even when comparing the results against the "combined" $LPM2_1$, $WFG2_1$, and $EMP2_1$ methods that incorporate the estimates from both radar sites (see Figs. $11a_3$–c_3). The RMS errors estimated are 0.24, 0.39, and 0.37 m for $LPM2_2$, $WFG2_2$, and $EMP2_2$, respectively, with the $LPM2_2$ derived data showing the highest correlation coefficient ($r = 0.85$) and a regression slope of 0.87 (see Table 3). The data inverted using these methods represent 47% and 27% of the record when swell was present for $LPM2_2$/$WFG2_2$ and $EMP2_2$, respectively (see Table 3).

d. Wind-wave spectrum inversion

In this section, the results from applying the Alattabi et al. (2019) wind-wave inversion module [Eq. (22)] are presented. Alattabi et al. (2019) suggested that Eq. (22) might have universal applicability with a regression coefficient of the value of $\alpha_w = 0.255 \pm 0.015$. This is first verified with the data from this study using the 12-MHz HF radar systems.

Following Alattabi et al. (2019) the dependence of the calibration coefficient on wind-wave frequency is examined using the wind-wave part of the radar Doppler spectral estimates and the in situ wave spectra with energy above the spectral noise floor that is assumed to be $0.15\ m^2\ Hz^{-1}$. The latter was defined after an examination of the in situ wave spectra. The data quality criteria (i.e., energy levels for first σ_1 and second-order peaks must be greater than 10 and 5 dB, respectively, and first-order energy at least 2 dB higher than the mean of the 1/3 highest second-order peaks, see section 4) are used for selecting the Doppler spectra to determine the coefficient required to invert for wind waves. The normalized weighted second-order spectral data [$R_W(f)$] were estimated from both radar sites (PEN and PER) using Doppler spectra corresponding to the buoy location and they are shown in Fig. 12 in the form of time-stack diagrams. The estimated $R_W(f)$ values correspond to discreet frequency bands that span the range of frequencies from the swell cutoff (f_c, see black line in Fig. 12) to 0.35 Hz. These were interpolated to match the frequency bands corresponding to the in situ wave spectra $S(f)$ estimates, which are limited to f_c and 0.35 Hz. Calibration coefficients $\alpha(f)$ were estimated for each wave frequency (f), as in Alattabi et al. (2019), using a least squares fit between all $S(f_i)$ and $R_W(f_i)$ values from all Doppler spectra and for each frequency band i within the wind-wave frequency range only, and the results are shown in Fig. 13.

TABLE 4. List of wind-wave coefficient a_w estimates for use with the empirical wind-wave inversion algorithm [see Eq. (22)] reported in this and previous studies. The corresponding radar frequencies are also listed.

Study	Radar frequency (MHz)	a_w
Heron and Heron (1998)	25.4	0.30
Ramos et al. (2009)	25.4	0.34
Alattabi et al. (2019)	48	0.25
This study	12	0.32

The coefficients estimated (see Fig. 13) for each site are similar to each other, independent on wave frequency. In the wave frequency range (0.05–0.2 Hz) the coefficients obtained are of similar magnitude across the wind-wave frequency range, independently of the site used. Furthermore, the frequency averaged values of the wind-wave regression coefficients, $\alpha_w = 0.37 \pm 0.012$ and 0.26 ± 0.04 for PEN and PER sites are close to that estimated in Alattabi et al. (2019) using a 48 MHz as well as to other empirical studies used weighting function $W(f)$ (see Fig. 13 and Table 4). This suggests that the wind-wave regression coefficient is not radar frequency dependent and a frequency and site averaged value of 0.32 ± 0.02 is estimated as long as the second-order Doppler spectrum is weighted using Barrick's weighting function. Here the averaged value of wind-wave regression coefficients from all studies listed in Table 4 is estimated and the value $\alpha_w = 0.3$ is adopted for the inversion of the wind-wave spectrum using Eqs. (22) and (23).

e. Hybrid method to estimate total wave spectrum

The $LPM2_2$ method has shown the best overall performance (see section 5c) as it provided a higher number of successful inversions than the other methods and the best accuracy in swell height estimates (RMS error of 0.24 m). Therefore, this method is adopted for estimating swell frequency, direction, and height from the Doppler spectra. These parameters are then used to reconstruct the swell spectrum assuming a Gaussian distribution (Alattabi et al. 2019) of the energy within the swell frequency band with the peak energy centered at the inverted swell frequency (f_s):

$$S_{sw}(f) = (H_{sw}^2/8\sqrt{2\pi\sigma^2})e^{-(f-f_s)^2/2\sigma^2}, \quad (34)$$

where σ is the width of the swell spectrum and $f < f_c$. The value of σ can be determined from historical data from the area, if available, or from validated model results (e.g.,

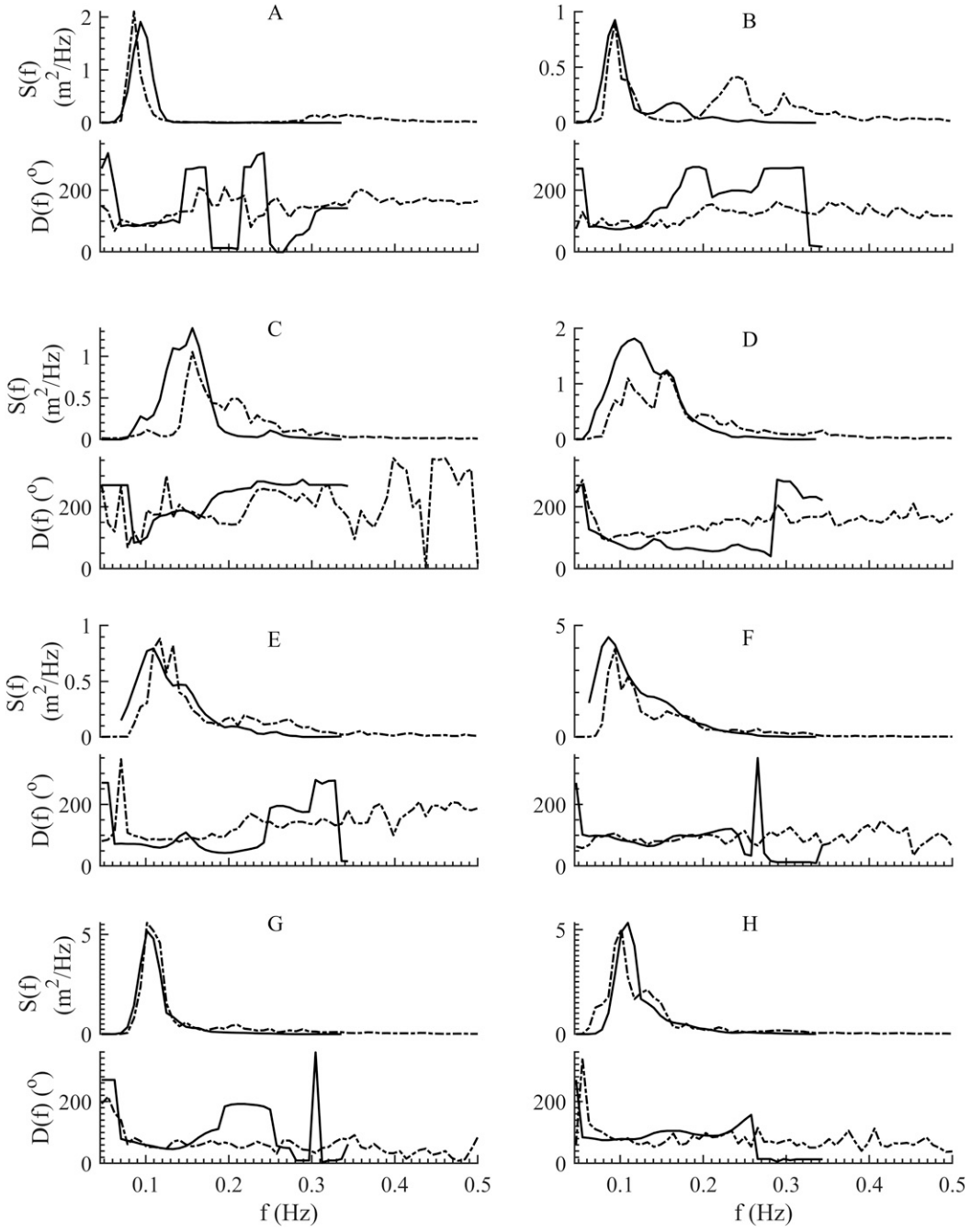

FIG. 14. Comparison of inverted (solid lines) and in situ (dashed lines) wave energy $S(f)$ and mean direction $D(f)$ spectra for events A to H. The total inverted wave energy spectra are obtained using the LPM2$_2$ method for swell and the average of the wind-wave spectra from the two sites (PEN and PER).

Kumar et al. 2017). Here, we used the value of 0.011. If the method failed to provide swell estimations, then it is assumed that no swell wave is present and the parameters $\sum R_W(f_i < f_c)$ and $S_{sw}(f)$ are set to zero.

After reconstructing the swell $S_{sw}(f)$ and wind-wave $S_{ww}(f)$ spectra, these are combined to a single one-dimensional spectrum inv.S(f) as follows (Alattabi et al. 2019):

$$\text{inv.S}(f) = \begin{cases} S_{sw}(f < f_c) + S_{ww}(f \geq f_c), & \text{if} \quad r \geq 0.3 \\ S_{ww}(f), & \text{if} \quad r < 0.3 \end{cases}, \tag{35}$$

$$r = \frac{\sum R_W(f_i < f_c)}{\sum R_W(f_i \geq f_c)}, \tag{36}$$

where f_c is the swell–wind-wave separation frequency determined using the wind speed and wave age (see section 4).

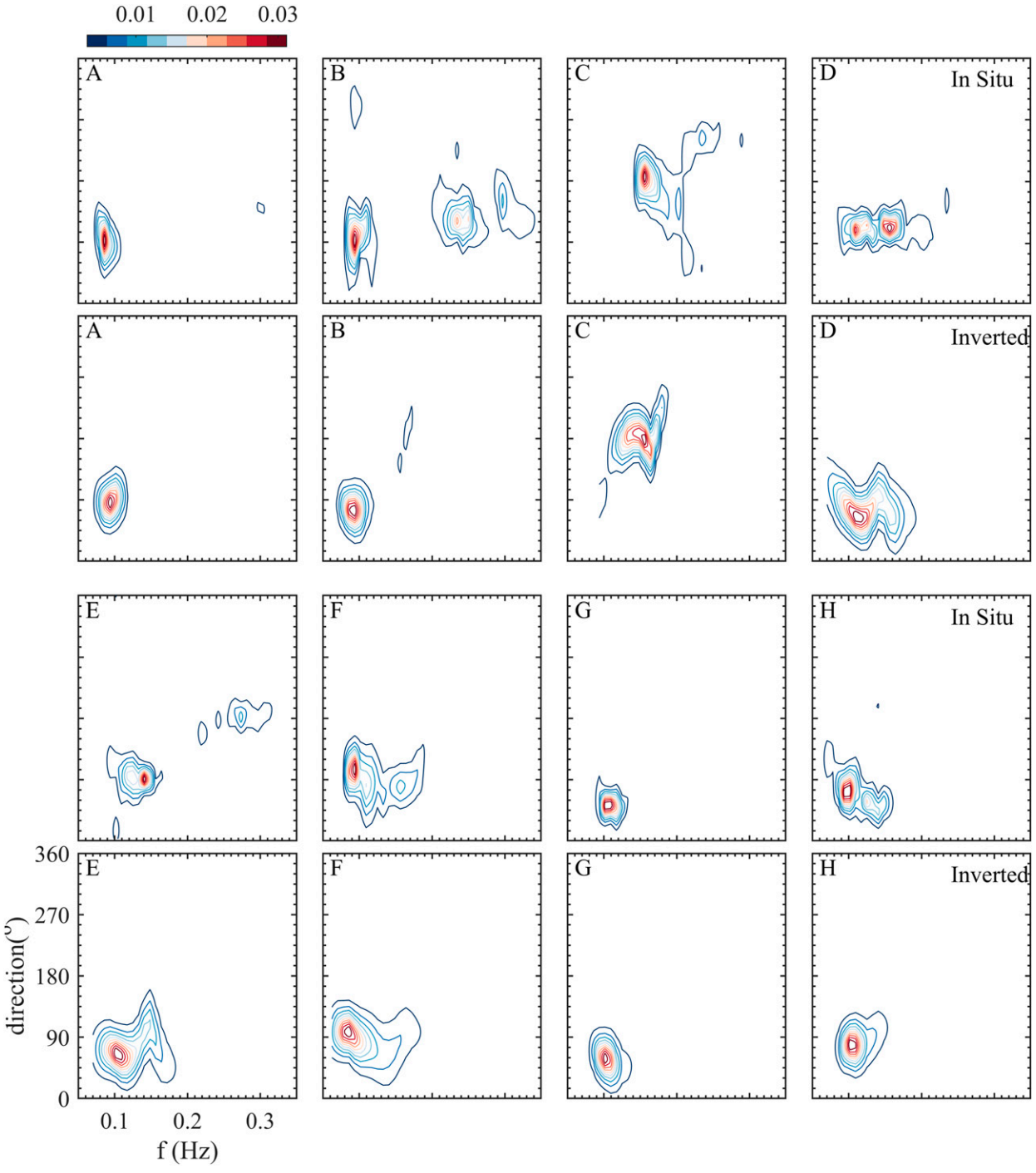

FIG. 15. Comparison of full directional inverted [Inv.S(f, θ)] and in situ [InSitu $S(f, \theta)$] spectra for events A–H.

The critical value of 0.3 in Eq. (35) was selected after trial and error as smaller values tended to indicate the presence of swell even when this was not present in the in situ record. When r <0.3 or $S_{sw} = 0$ (when swell peaks are not found), the inverted wind-wave spectrum is used for the entire range of frequencies including the swell band ($f_i < f_c$).

Bulk inverted wave parameters are calculated by integrating the total inverted wave spectrum inv.S(f) over the range 0.046–0.35 Hz with spectral resolution of 0.0078 Hz.

1) ONE-DIMENSIONAL WAVE SPECTRA

The ability of the inversion method to estimate the one-dimensional wave spectra is demonstrated in Fig. 14, where

TABLE 5. Statistical comparison of in situ and inverted estimates of total and wind-wave RMS wave height, mean and peak frequency, and direction (see Fig. 16). The root-mean-square (RMS error, correlation coefficient (r) for wave height, frequency estimates and direction (complex, shown as r and angle). In addition, regression slope, normalized RMS error (NRMS), scatter index (SI), corrected indicator (HH), and bias (BI) are listed for wave heights and frequencies. Note that in this comparison 626 data points are used; that corresponds to 93% of the total data available.

	Parameter	RMS error	r	Angle (°)	Slope	NRMS error	SI	HH	BI
Total	$H_{\rm rms}$	0.35 m	0.92	—	1.02	0.21	0.21	0.21	0.03
	f_P	0.03 Hz	0.63	—	0.85	0.25	0.24	0.27	−0.01
	f_m	0.02 Hz	0.55	—	0.82	0.22	0.15	0.24	−0.02
	Peak direction	46°N	0.57	19	—	—	—	—	—
	Mean direction	38°N	0.72	15	—	—	—	—	—
Wind wave	$H_{\rm rms}$	0.34 m	0.93	—	1.11	0.26	0.25	0.25	0.12
	f_P	0.04 Hz	0.66	—	0.80	0.28	0.24	0.32	−0.02
	f_m	0.03 Hz	0.73	—	0.82	0.21	0.13	0.23	−0.03
	Peak direction	43°	0.70	18	—	—	—	—	—
	Mean direction	41°	0.78	15	—	—	—	—	—
Wind	Wind direction	72°	0.60	−4	—	—	—	—	—

inverted spectra (solid lines) corresponding to events A–H are shown together with the in situ spectra (dashed lines). As described earlier (see Figs. 5 and 7), these events are examples of only swell (A, G, and H), only wind (C), and mixed wave conditions (B, D, E, and F). Overall, the high energy peaks in the inverted spectra agree overall in both magnitude and frequency location with the in situ peak spectra, although in cases B, C, and E, the inverted spectra fail to identify the secondary wind-wave peaks present at higher frequencies.

2) MEAN DIRECTION AS FUNCTION OF FREQUENCY

The estimation of mean direction as a function of wave frequency is carried out using Eq. (29) (see section 2c) with Doppler spectra from both radar sites PEN and PER using their corresponding beams aiming at the buoy location. An example of inverted mean direction as function of frequency is shown in Fig. 14 for events A–H (solid lines) together with the in situ directions estimated using the buoy data (dashed lines). The method seems to provide accurate estimates at least for the frequencies where significant wave energy has been identified in the inverted energy spectrum (see Fig. 14).

3) FULL DIRECTIONAL WAVE SPECTRA

The directional wave spectra inv.S(f, θ) are constructed using Eqs. (28)–(30) and using the inverted total wave inv.S(f) and mean direction $\theta(f)$ spectra. The peak frequency identified on the inv.S(f) is used to determine the value of β for the distribution function [see Eqs. (29) and (30), section 2e]. The results of inverted directional frequency spectra for events A to H are shown in Fig. 15 together with the corresponding in situ directional spectra. Except for events B, C, and E, the remaining of the events show good agreement with in situ data, in terms of both wave energy levels and peak energy location.

4) BULK WAVE PARAMETERS

In comparing our estimates with the in situ data, we report the RMS error as in previous studies. However, since the RMS error always depends on the magnitude of the wave conditions, we also report the normalized root-mean-square error (NRMS) as well as scatter index (SI). Mentaschi et al. (2013) argued that these parameters might not reflect accurate performance, especially in cases of negative bias, and suggested using the corrected indicator of Hanna and Heinold (1985), denoted as HH. The latter parameter is also estimated and listed in Table 5.

Wave height, peak, and mean wave frequencies determined from the inverted total wave height spectra are compared to the in situ wave parameters in Fig. 16 and Table 5. For the period of the experiment (total wave heights: 0.29–5.1 m; mean wave height: 1.4 m) the RMS error of total wave height is 0.35 m, correlation coefficient r = 0.92, and SI of 0.21. The inverted mean frequency estimation agrees better with the in situ data than the peak frequency as their corresponding RMS errors are 0.02 and 0.03 Hz. The correlation coefficients for the mean and peak frequency estimates are 0.55 and 0.63, respectively, while the slopes of the regression lines (<0.85) suggest some underestimation. Mean wave direction estimates appear to be slightly better than peak direction estimates with an RMS error of 38° and a complex correlation coefficient $|r|$ of 0.72 and angle 15°. The corresponding values for peak direction are 46°, 0.57, and 19°, respectively. Wind direction estimates are the least accurate with a relatively high RMS error (~72°) and a complex correlation coefficient with magnitude of 0.60 and angle of −4° (see Table 5).

The inverted wind-wave spectra are used to estimate the corresponding inverted wind-wave RMS wave height, peak and mean wave frequencies, and directions. These are compared to the partitioned parameters from in situ spectra and the scatterplots and the statistics of this comparison are shown in Fig. 16 (red dots) and Table 5, respectively. The RMS error in wind-wave height is 0.34 m with correlation coefficient of 0.93 and SI of 0.25. Peak frequencies show error of 0.04 Hz with a correlation coefficient of 0.66, while the mean frequency errors are slightly improved (RMS error of 0.03 Hz and r = 0.73). The slopes of the regression lines suggest that mean and peak frequencies are underestimated (slope ≤ 0.82). The peak

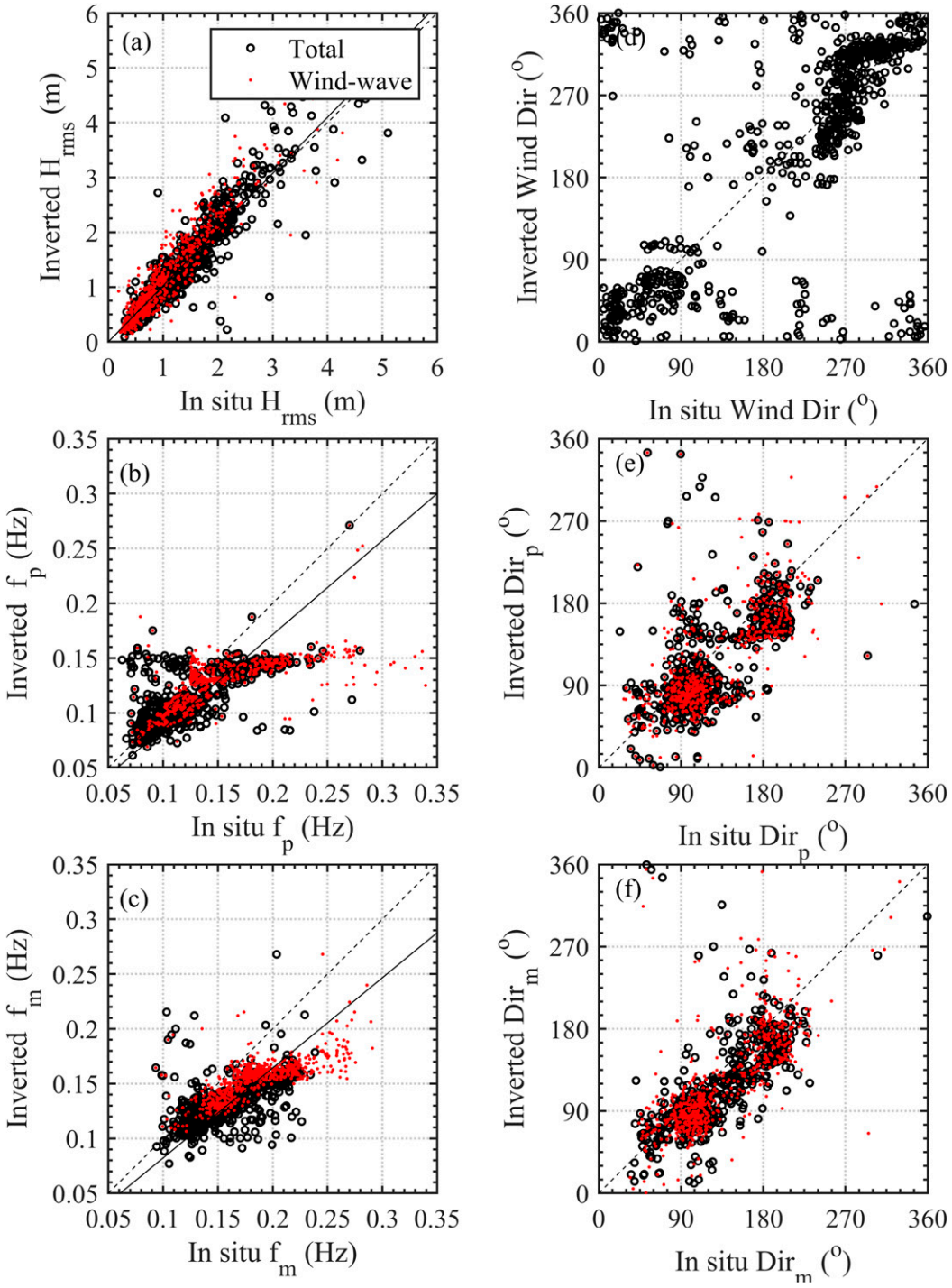

FIG. 16. Comparison of wave bulk parameters, (a) RMS wave height, (b),(c) peak and mean wave frequency, (d) wind direction, and (e),(f) peak and mean wave directions using beams from two sites (PEN and PER). Black circles represent total (swell and wind waves) while red dots represent wind waves only. The 1:1 (dashed) and the best-fit (solid) lines are also shown while the statistics are listed in Table 5.

TABLE 6. Comparison of the performance of the swell inversion method (LPM) to estimate swell wave height using inverted (LPM) and measured (⟨LPM⟩) swell frequency (f_s) and direction (θ_{sw}) as described in section 6a. The comparisons of inverted vs in situ swell height are presented in terms of RMS error (in m), correlation coefficients (r), and regression slope. N is number of data points used.

No. of sites and beams used	Model	Site	Beam 1 (°N)	Beam 2 (°N)	N	%	RMS error (m)	r	Slope
One site–one beam	LPM1, Eq. (6)	PEN	13	—	116	21	0.94	0.53	1.23
		PER	271	—	154	28	0.75	0.53	1.26
	⟨LPM1⟩	PEN	13	—	262	48	0.56	0.44	0.86
		PER	272	—	433	80	0.71	0.44	1.12
One site–two beams	$LPM2_1$, Eqs. (10) and (11)	PEN	28	355	170	31	0.45	0.77	0.54
		PER	287	256	130	24	0.41	0.73	0.75
	$\langle LPM2_1 \rangle$	PEN	28	355	92	17	0.53	0.63	0.72
		PER	287	256	340	63	0.57	0.47	1.01
Two sites–two beams	$LPM2_2$, Eqs. (10) and (11)	PEN and PER	13	272	253	47	0.24	0.85	0.87
	$\langle LPM2_2 \rangle$	PEN and PER			125	23	0.31	0.78	0.95

direction has an RMS error of 43° with complex correlation coefficient $|r|$ of 0.70 and angle 18°, while RMS error of 41° with $|r| = 0.78$ and angle 15° are found in mean direction comparisons.

6. Discussion

a. *Inverted swell parameters from LPM swell inversion method*

The results of swell inversion (section 5c) suggest that the $LPM2_2$ method (Lipa et al. 1981) performs better than the other two methods (WFG and EMP). Although the application of the method was explored using different combinations of radar sites and beams (i.e., one site–one beam, one site–two beam, and two sites–two beams), use of two beams from two different sites ($LPM2_2$) provided the most accurate swell wave heights and performed better than LPM1 and $LPM2_1$. This is attributed to the fact that use of this method ensures that both beams from the two stations pointed at the same location (buoy site) and as such they describe the same patch of the ocean. This is not the case for $LPM2_1$ scenario, where the two beams from a single site provide backscatter from different patches of the ocean. In the two sites–two beams scenario, the PEN and PER beams are almost perpendicular to each other (99°) while the angle of the beams used in $LPM2_1$ is only 30°. This low angle does not seem to be suitable to allow adequate resolution of the swell waves in the Doppler spectra.

Although the LPM method was found to perform best for swell height, it was not successful in estimating swell direction. Estimation of swell wave height requires knowing swell direction and frequency, which are used within the coupling coefficient equation. The importance of these two parameters that are obtained through inversion is examined through a sensitivity analysis. For this analysis, the swell frequency and direction values from the in situ data are used (instead of the inverted ones) to estimate swell heights with the LPM method. The results from this exercise, denoted as ⟨LPM⟩, are compared to the original swell height estimates using LPM1, $LPM2_1$, and $LPM2_2$ (see Table 6). The resulting swell heights, from either LPM1, $LPM2_1$, or $LPM2_2$, do not seem to be significantly different, suggesting that swell height estimates do not depend heavily on the accuracy of the inverted swell frequency and direction. For instance, the use of in situ data in the $LPM2_2$ method provided wave heights with RMS error of 0.31 m and a correlation coefficient $r = 0.78$, while the original $LPM2_2$ method shows better agreement (see Table 6). The same situation can be seen for the other two methods. Since swell frequency and direction do not seem to be responsible for the errors in swell height estimates, it is concluded that identifying the swell peak energy in the Doppler spectrum R_j [see Eq. (33)] is most important. Errors in estimating R_j can be due to noisy Doppler spectrum but most likely it relates to the limits used to integrate the swell energy in the Doppler spectrum and to define the energy of the first-order peak. In this study a constant cutoff of 0.046 Hz was used that might not be always appropriate.

b. *Inverted bulk wave parameters*

The time series of inverted total and swell wave parameters are shown in Fig. 17 and these include data with swell cross angle $> 75°$. In Figs. 17b, 17e, and 17h, the $LPM2_2$ inverted swell parameters are shown. In there, the cases with swell cross angle $> 75°$ are identified with green triangle symbols and show that these instances correspond to overestimated swell wave heights. However, total wave height estimates are in good agreement with the in situ values. Although an agreement is found in the estimates of mean and peak wave frequency the inversion method provides slightly underestimated values (see Figs. 17e–f). This is similar to the findings of Lopez and Conley (2019) who also noted underestimations in frequency estimates.

The lack of inverted values (Figs. 17a–i) is attributed mostly to failure of the swell inversion when 1) no swell peaks were identified in the Doppler spectrum (49% of the in situ swell record) and 2) Doppler spectra do not satisfy the QA criteria required (6% of the in situ swell record). The estimation of wind direction is shown in Fig. 17j and

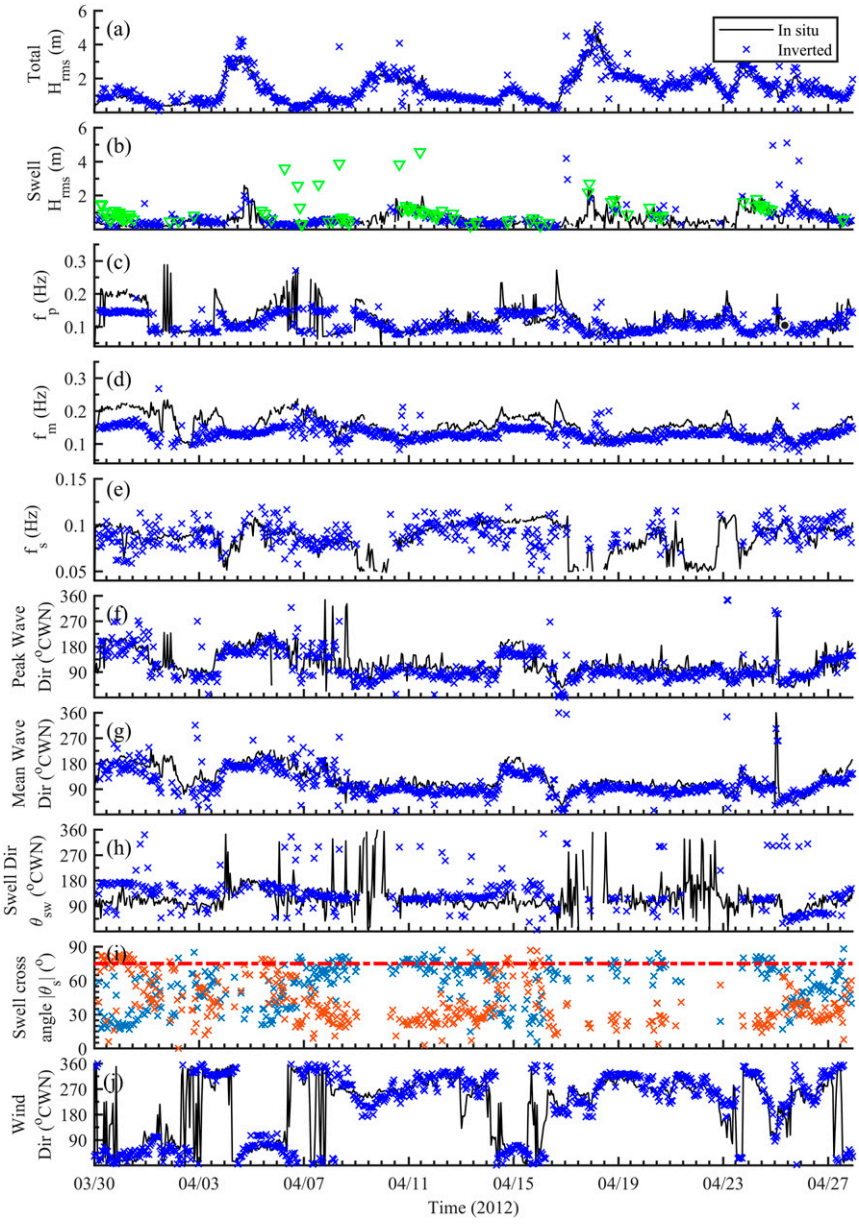

FIG. 17. Time series comparison of in situ (black) and inverted (blue) total and swell wave parameters using data from two sites–two beams ($LPM2_2$ method) including data with swell cross angle $|\theta_s| > 75°$: (a) total (wind and swell) RMS wave height, (b) swell RMS wave height (green triangles denote data when $|\theta_s| > 75°$), (c) peak frequency, (d) mean wave frequency, (e) swell frequency, (f) peak direction, (g) mean wave direction, (h) swell only direction, (i) swell cross angle for PEN (blue) and PER (red) beams, and (j) wind direction. Note that the white gaps in total and swell results are attributed to Doppler spectra that did not pass the quality criteria (see text for details) as well as to cases where no swell was detected by the radar.

shows good agreement with the in situ data. The differences in data availability for wave inversion and wind direction estimations are attributed to the fact that the wind direction method relies only on the Bragg peak energy that needs to be well above the noise level. This is not always the case for the second-order peaks used for swell and wind-wave inversion.

The performance of the wave inversion method presented in this study is examined by comparing the results with those from other theoretical and empirical wave inversion studies (see Table 7). Our method shows to perform well, and the estimates of total wave height have RMS error of 0.35 m, $r = 0.92$, and SI of 0.21. These values are comparable and often better than the errors reported using more complicated theoretical wave

TABLE 7. Comparison of the performance of the hybrid model presented in this study with other (theoretical and empirical) wave inversion methods reported in the literature. Root-mean-square errors (RMSE) and correlation coefficients (r) of total wave height and peak and mean wave period estimated using in situ measurements are listed.

			H_{rms} (m)		T_P (s)		T_m (s)	
Inversion type	Study	f_{radar} (MHz)	RMSE (m)	r	RMSE (s)	r	RMSE (s)	r
Theoretical	Wyatt et al. (2006)	7–10	0.19–0.46	0.55–0.94	—	—	1.27–4.56	0.13–0.81
	Wyatt et al. (2009)	16	0.28–0.32	0.96–0.97	—	—	—	—
	Hisaki (2016)	24.5	0.15–0.86	0.63–0.76	—	—	0.26–0.95	0.69–0.82
	Saviano et al. (2019)	25	0.23–0.66	0.50–0.75	—	—	—	—
Empirical	Chen et al. (2013)	7.5–25	0.19–1.29	0.45–0.82	—	—	—	—
	Gomez et al. (2015)	12	0.25–0.48	0.78–0.93	1.46–4.23	0.33–0.76	0.81–2.81	0.52–0.81
	Middleditch (2013)	8.34	0.36–0.70	0.35–0.51	0.89–2.44	0.3–0.57	0.72–1.26	0.28–0.50
	Ramos et al. (2009)	25.4	0.14–0.50	0.68–0.95	—	—	—	—
	Lopez et al. (2016)	12	0.26–0.44	0.90–0.96	—	—	—	—
	Lopez and Conley (2019)	12.3	0.30–0.45	0.87–0.94	—	—	—	—
	Alattabi et al. (2019)	48	0.16–0.25	0.86–0.94	1.38–2.16	0.51–0.84	0.79–0.84	0.80–0.95
Semi-empirical	This study	12	0.35	0.92	2.1	0.63	0.88	0.55

inversion techniques (see Table 7). For mean and peak frequency estimations, it seems most inversion methods including this study show a similar, fair correlation with the in situ data (see Table 7).

c. *Inverted wave and directional wave spectra*

The inverted and in situ directional and nondirectional wave spectra for events A–H (Figs. 14 and 15) show strong agreements. The nondirectional wave spectra agree in terms of energy content for most events except B, C, and E (Fig. 14). During these events, the in situ spectra show secondary energy peaks at ~0.24 Hz; these peaks are not present in the inverted spectra. This is attributed to the weighting function $W(f)$ used in forming the normalized second-order spectra $R_W(f)$ [see Eq. (23)]. Its purpose is to reduce the effects of second harmonic and corner reflection peaks generated by the interaction of EM and ocean waves (Barrick 1972; Ivonin et al. 2006) (see Figs. 3 and 18) that appear at $\pm 2^{1/2} f_B$ and $\pm 2^{3/4} f_B$ (see Fig. 3). Also, second harmonic peak can be seen in event B, where this peak is not present in situ spectra (see Fig. 14). However, this might have some undesirable effects that are further explored. As shown in Fig. 3, the weighting function for a 48-MHz radar shows the corner reflection peak to be at high wave frequencies (~0.49 Hz). For the 12 MHz system these undesirable peaks appear at frequencies 0.146 and 0.241 Hz, respectively (see Fig. 3), which are areas where significant wave energy might be present. In this case the weighting function would suppress the wave energy at these frequencies that can be seen both in the in situ spectra [$S(f)$] and in the nonweighted second-order spectra $R(f)$ corresponding to events B, C, and E (see Fig. 18). An example of a clear corner reflection effect can be seen in Fig. 18, cases F and H, where the unweighted normalized second-order spectra $R(f)$ at these events (F and H) contain a secondary peak at 0.24 Hz; its signature is not found in the in situ measurements (see Figs. 18f,h). This removal of wave energy is a limitation of applying the weighting function and its application should be critically examined. Despite this limitation the overall energy content of the inverted spectra is similar to that of the in situ wave spectra.

The accuracy of inverted wave parameters and directional wave spectra estimated from the inversion method developed in this study are similar to those reported in Lopez and Conley (2019) who used the more complicated inversion method of Wyatt (2000).

Some wave inversion studies use 0.25 Hz as the upper frequency limit for 12-MHz systems mainly due to the limitation of the inversion method used [for more details, see Lopez and Conley (2019) and Wyatt et al. (2011)]. In this study, we extended this limit to 0.35 Hz, and the inverted wave and directional wave spectra estimates were found to be satisfactory.

In addition to the limitations presented above, there is a relationship between HF radar frequency and range of swell cross angles at which singularities occur. This range increases with decreasing radar frequency (i.e., >60° for 4 MHz while >75° for 12 MHz) making this an important limitation for lower-frequency systems. As shown in section 6a the accuracy of the LPM method to estimate swell wave height is related to the method used to identify and accurately determine the swell peak energies R_j [see Eqs. (6) and (33)], something that depends on the limits used for defining the energy of the first-order peak especially when this is broad as this affects the lower limit of the swell band to be inverted. The technique could benefit from the development of more accurate and robust methods for estimating these cutoff frequency limits so that it avoids contamination of the swell band by first-order energy. Flagging these cases and reject them from inversion might be needed. The comparison of the three different beam/site combinations used in the application of the LPM method has revealed that: the use of two beams from a single site requires an angle between the two beams that is greater than 30°. As argued earlier, the assumption of homogeneity in the swell signal at the two beams might not be valid for longer ranges. In addition, this limits the allowed number of beams available from a single beam-forming radar where the radial coverage is limited to −60° to 60° from the radar boresight.

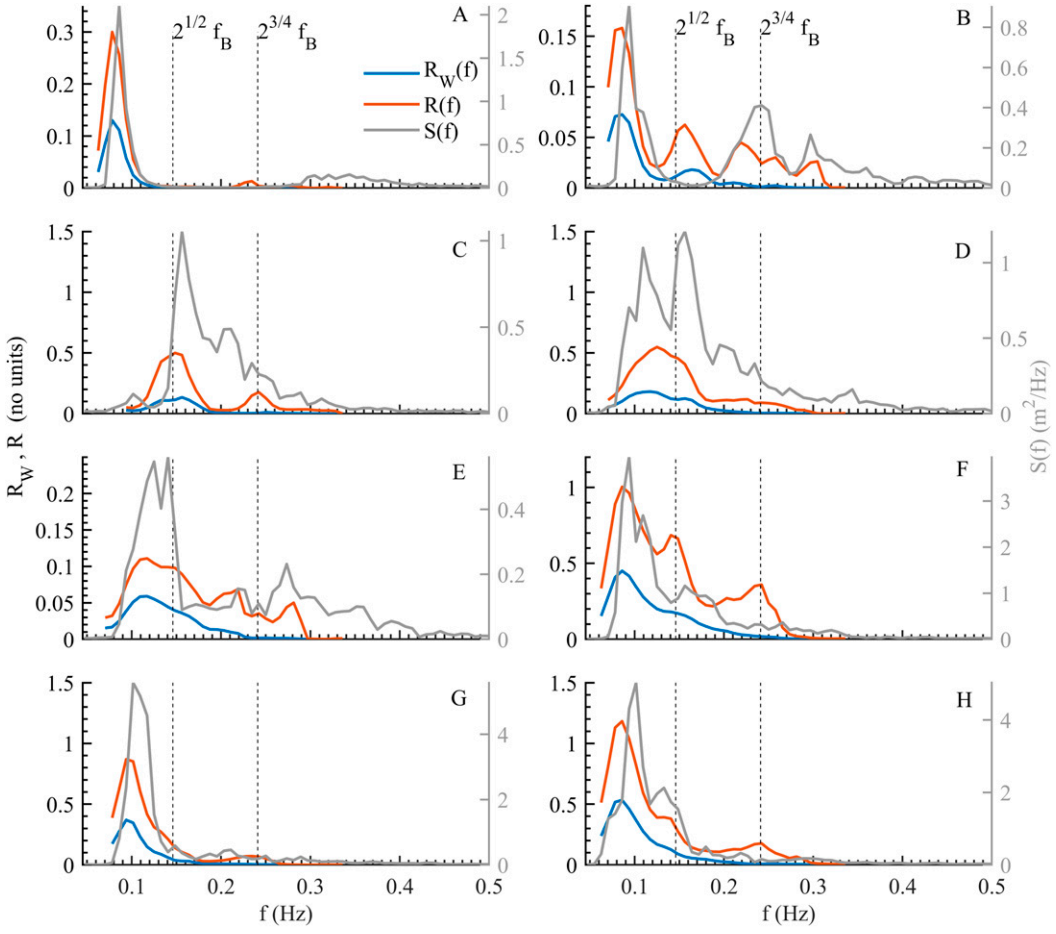

FIG. 18. Examples from A–H events showing the contribution of the weighting function in reducing the effect of the second harmonic and corner reflection peaks (located at $2^{1/2}f_B$ and $2^{3/4}f_B$, where f_B is the Bragg frequency) in the normalized second-order spectra $R_W(f)$ (blue). R (orange) is the unweighted normalized second-order spectra, and $S(f)$ (gray) denotes in situ wave spectra from wave buoy ($m^2\,Hz^{-1}$).

Furthermore, the inverted results from LPM method for one site–one beam show high reduction of data availability because it requires that all four swell peaks are available from a single Doppler spectrum, something that is not always possible. The LPM method performs best when Doppler spectra from two beams from two different sites are used.

7. Concluding remarks

In this manuscript, we introduced a relatively simple, semi-empirical method to estimate full wave and directional wave spectra from radar data even when swell is present. This method requires treating the wind-wave and swell inversions separately. The wind-wave spectra estimation is based on the empirical method introduced by Barrick (1977b), while the swell spectra estimation utilizes a simplified version of the theoretical swell inversion presented by Lipa et al. (1981) that was found to be better performing than the WFG (Wang et al. 2016) and EMP (swell empirical approach introduced in this study) methods. The LPM method was found to perform best when two beams from two different sites ($LPM2_2$) are used as long as the swell cross angle is below 75°, for the 12-MHz system used in this study.

The inversion of the wind-wave component is similar to that presented in Alattabi et al. (2019), and the regression coefficient α_w was consistent for the two systems used in the study (PEN and PER sites) (see Fig. 13). The value of 0.32 is found for α_w over ocean wave frequencies of 0.05–0.2 Hz. This value is similar to other wave inversion studies that include the weighting function derived by Barrick (1977b) and used different operating radar frequencies (see Table 4). This suggests that a constant value of 0.3 for wind-wave regression coefficient would be sufficient for universal application independent of operation frequency. Although the one-month dataset used in this manuscript might be considered short for comparisons and evaluations, it does capture different combinations of swell and wind waves ensuring a range of conditions. It is our anticipation and hope that this method would be further evaluated using different radar frequencies and using data covering longer periods.

The MATLAB scripts for implementation of the inversion model presented in this manuscript a [Swell Wave Inversion Code (SWaveRIC)] is available online (Al-Attabi et al. 2021).

Acknowledgments. The contribution of Mr. Douglas Cahl in providing support, insights, and assistance with some of the coding is greatly appreciated. The first author (Zaid R. Al-Attabi) was supported by a fellowship from the Higher Committee for Education Development (HCED) in Iraq. Additional support during data analysis and preparation of this manuscript was provided by the Southeast Coastal Observing Regional Association (SECOORA) pursuant to NOAA Award NA16NOS0120028. We would like to acknowledge the Natural Environmental Research Council (Grant NE/J004219/1) for their support of the Wave Hub HF Radar system and the efforts of Maxwell Bradbury in preparing the data used in this work. Manuscript preparation and finalization took place while G. Voulgaris was serving at the U.S. National Science Foundation. Any opinions, findings, and conclusions or recommendations expressed in here are those of the authors and do not necessarily reflect the views of any of the funding organizations.

REFERENCES

Alattabi, Z. R., D. Cahl, and G. Voulgaris, 2019: Swell and wind wave inversion using a single very high frequency (VHF) radar. *J. Atmos. Oceanic Technol.*, **36**, 987–1013, https://doi.org/10.1175/JTECH-D-18-0166.1.

——, ——, and ——, 2021: Swell Wave Radar Inversion Code (SWaveRIC). Zenodo, accessed 4 August 2021, https://doi.org/10.5281/zenodo.5159956.

Barrick, D. E., 1971: Theory of HF and VHF propagation across the rough sea, 1, The effective surface impedance for a slightly rough highly conducting medium at grazing incidence. *Radio Sci.*, **6**, 517–526, https://doi.org/10.1029/RS006i005p00517.

——, 1972: Remote sensing of sea state by radar. *Ocean 72-IEEE Int. Conf. on Engineering in the Ocean Environment*, Newport, RI, IEEE, 186–192, https://doi.org/10.1109/OCEANS.1972.1161190.

——, 1977a: The ocean wave height nondirectional spectrum from inversion of the HF sea-echo Doppler spectrum. *Remote Sens. Environ.*, **6**, 201–227, https://doi.org/10.1016/0034-4257(77)90004-9.

——, 1977b: Extraction of wave parameters from measured HF radar sea-echo Doppler spectra. *Radio Sci.*, **12**, 415–424, https://doi.org/10.1029/RS012i003p00415.

——, and B. Weber, 1977: On the nonlinear theory for gravity waves on the ocean's surface. Part II: Interpretation and applications. *J. Phys. Oceanogr.*, **7**, 11–21, https://doi.org/10.1175/1520-0485(1977)007<0011:OTNTFG>2.0.CO;2.

Bathgate, J. S., M. L. Heron, and A. Prytz, 2006: A method of swell wave parameter extraction from HF ocean surface radar spectra. *IEEE J. Oceanic Eng.*, **31**, 812–818, https://doi.org/10.1109/JOE.2006.886237.

Bidlot, J., 2001: ECMWF wave model products. *ECMWF Newsletter*, No. 91, ECMWF, Reading, United Kingdom, 9–15, https://www.ecmwf.int/sites/default/files/elibrary/2001/14633-newsletter-no91-summer-2001.pdf.

Cahl, D., and G. Voulgaris, 2019: WavePART V.1.1 MATLAB(r) software for the partition of directional ocean wave spectra. Zenodo, accessed 13 April 2019, https://doi.org/10.5281/zenodo.2638501.

Chen, Z., C. Zezong, J. Yanni, F. Lingang, and Z. Gengfei, 2013: Exploration and validation of wave-height measurement using multifrequency HF radar. *J. Atmos. Oceanic Technol.*, **30**, 2189–2202, https://doi.org/10.1175/JTECH-D-12-00178.1.

——, L. Zhang, C. Zhao, X. Chen, and J. Zhong, 2015: A practical method of extracting wind sea and swell from directional wave spectrum. *J. Atmos. Oceanic Technol.*, **32**, 2147–2159, https://doi.org/10.1175/JTECH-D-15-0092.1.

Churchill, J. H., A. J. Plueddemann, and S. M. Faluotico, 2006: Extracting wind sea and swell from directional wave spectra derived from a bottom-mounted ADCP. Woods Hole Oceanographic Institution Tech Rep. WHOI-2006-13, 41 pp., https://doi.org/10.1575/1912/1372.

Crombie, D. D., 1955: Doppler spectrum of sea echo at 13.56 Mc./s. *Nature*, **175**, 681–682, https://doi.org/10.1038/175681a0.

De Farias, E. G., J. A. Lorenzzetti, and B. Chapron, 2012: Swell and wind-sea distributions over the mid-latitude and tropical North Atlantic for the period 2002–2008. *Int. J. Oceanogr.*, **2012**, 306723, https://doi.org/10.1155/2012/306723.

Donelan, M. A., J. Hamilton, and W. H. Hui, 1985: Directional spectra of wind-generated ocean waves. *Proc. Roy. Soc. London*, **A315**, 509–562, https://doi.org/10.1098/rsta.1985.0054.

Earle, M., 1984: Development of algorithms for separation of sea and swell. National Data Buoy Center Tech. Rep. MEC-87-1, 53 pp.

Essen, H.-H., K.-W. Gurgel, and T. Schlick, 1999: Measurement of ocean wave height and direction by means of HF radar: An empirical approach. *Dtsch. Hydrogr. Z.*, **51**, 369–383, https://doi.org/10.1007/BF02764161.

Fernandez, D. M., H. C. Graber, J. D. Paduan, and D. E. Barrick, 1997: Mapping wind direction with HF radar. *Oceanography*, **10**, 93–95, https://doi.org/10.5670/oceanog.1997.33.

Gilhousen, D. B., and R. Hervey, 2002: Improved estimates of swell from moored buoys. *Fourth Int. Symp. on Ocean Wave Measurement and Analysis*, San Francisco, CA, American Society of Civil Engineers, 387–393, https://doi.org/10.1061/40604(273)40.

Gill, E. W., 1990: An algorithm for the extraction of ocean wave parameters from wide beam HF radar (CODAR) backscatter. Ph.D. dissertation, Memorial University of Newfoundland, 267 pp.

Gomez, R., T. Helzel, L. Wyatt, G. Lopez, D. Conley, N. Thomas, S. Smet, and G. Sicot, 2015: Estimation of wave parameters from HF radar using different methodologies and compared with wave buoy measurements at the Wave Hub. *OCEANS 2015—Genova*, Genoa, Italy, IEEE, https://doi.org/10.1109/OCEANS-Genova.2015.7271477.

Gurgel, K.-W., H. H. Essen, and T. Schlick, 2006: An empirical method to derive ocean waves from second-order Bragg scattering: Prospects and limitations. *IEEE J. Oceanic Eng.*, **31**, 804–811, https://doi.org/10.1109/JOE.2006.886225.

Hanna, S. R., and D. W. Heinold, 1985: Development and application of a simple method for evaluating air quality models. American Petroleum Institute Publ. 4409, 38 pp.

Hanson, J. L., and O. M. Phillips, 2001: Automated analysis of ocean surface directional wave spectra. *J. Atmos. Oceanic Technol.*, **18**, 277–293, https://doi.org/10.1175/1520-0426(2001)018<0277:AAOOSD>2.0.CO;2.

Hasselmann, D. E., M. Dunckel, and J. Ewing, 1980: Directional wave spectra observed during JONSWAP 1973. *J. Phys. Oceanogr.*, **10**, 1264–1280, https://doi.org/10.1175/1520-0485(1980)010<1264:DWSODJ>2.0.CO;2.

Hasselmann, K., 1971: Determination of ocean wave spectra from Doppler radio return from the sea surface. *Nat. Phys. Sci.*, **229**, 16–17, https://doi.org/10.1038/physci229016a0.

Herbers, T., S. Elgar, and R. Guza, 1999: Directional spreading of waves in the nearshore. *J. Geophys. Res.*, **104**, 7683–7693, https://doi.org/10.1029/1998JC900092.

Heron, M., and R. Rose, 1986: On the application of HF ocean radar to the observation of temporal and spatial changes in wind direction. *IEEE J. Oceanic Eng.*, **11**, 210–218, https://doi.org/10.1109/JOE.1986.1145173.

——, and A. Prytz, 2002: Wave height and wind direction from the HF coastal ocean surface radar. *Can. J. Remote Sens.*, **28**, 385–393, https://doi.org/10.5589/m02-031.

——, P. Dexter, and B. McGann, 1985: Parameters of the air-sea interface by high-frequency ground-wave Doppler radar. *Mar. Freshwater Res.*, **36**, 655–670, https://doi.org/10.1071/MF9850655.

Heron, S., and M. Heron, 1998: A comparison of algorithms for extracting significant wave height from HF radar ocean backscatter spectra. *J. Atmos. Oceanic Technol.*, **15**, 1157–1163, https://doi.org/10.1175/1520-0426(1998)015<1157:ACOAFE>2.0.CO;2.

Hessner, K., and J. L. Hanson, 2010: Extraction of coastal wavefield properties from X-band radar. *2010 IEEE Int. Geoscience and Remote Sensing Symp.*, Honolulu, HI, IEEE, 4326–4329, https://doi.org/10.1109/IGARSS.2010.5650134.

Hildebrand, P. H., and R. Sekhon, 1974: Objective determination of the noise level in Doppler spectra. *J. Appl. Meteor.*, **13**, 808–811, https://doi.org/10.1175/1520-0450(1974)013<0808:ODOTNL>2.0.CO;2.

Hisaki, Y., 1996: Nonlinear inversion of the integral equation to estimate ocean wave spectra from HF radar. *Radio Sci.*, **31**, 25–39, https://doi.org/10.1029/95RS02439.

——, 2016: Ocean wave parameters and spectrum estimated from single and dual high-frequency radar systems. *Ocean Dyn.*, **66**, 1065–1085, https://doi.org/10.1007/s10236-016-0978-3.

Howell, R., and J. Walsh, 1993: Measurement of ocean wave spectra using narrow-beam HE radar. *IEEE J. Oceanic Eng.*, **18**, 296–305, https://doi.org/10.1109/JOE.1993.236368.

Ivonin, D. V., V. I. Shrira, and P. Broche, 2006: On the singular nature of the second-order peaks in HF radar sea echo. *IEEE J. Oceanic Eng.*, **31**, 751–767, https://doi.org/10.1109/JOE.2006.886080.

Kumar, N., D. L. Cahl, S. C. Crosby, and G. Voulgaris, 2017: Bulk versus spectral wave parameters: Implications on stokes drift estimates, regional wave modeling, and HF radars applications. *J. Phys. Oceanogr.*, **47**, 1413–1431, https://doi.org/10.1175/JPO-D-16-0203.1.

Lipa, B. J., 1977: Derivation of directional ocean-wave spectra by integral inversion of second-order radar echoes. *Radio Sci.*, **12**, 425–434, https://doi.org/10.1029/RS012i003p00425.

——, and D. E. Barrick, 1980: Methods for the extraction of long period ocean wave parameters from narrow beam HF radar sea echo. *Radio Sci.*, **15**, 843–853, https://doi.org/10.1029/RS015i004p00843.

——, ——, and J. W. Maresca, 1981: HF radar measurements of long ocean waves. *J. Geophys. Res.*, **86**, 4089–4102, https://doi.org/10.1029/JC086iC05p04089.

Long, A., and D. Trizna, 1973: Mapping of North Atlantic winds by HF radar sea backscatter interpretation. *IEEE Trans. Antennas Propag.*, **21**, 680–685, https://doi.org/10.1109/TAP.1973.1140557.

Longuet-Higgins, M. S., 1963: The effect of non-linearities on statistical distributions in the theory of sea waves. *J. Fluid Mech.*, **17**, 459–480, https://doi.org/10.1017/S0022112063001452.

Lopez, G., and D. C. Conley, 2019: Comparison of HF radar fields of directional wave spectra against in situ measurements at multiple locations. *J. Mar. Sci. Eng.*, **7**, 271, https://doi.org/10.3390/jmse7080271.

——, ——, and D. Greaves, 2016: Calibration, validation, and analysis of an empirical algorithm for the retrieval of wave spectra from HF radar sea echo. *J. Atmos. Oceanic Technol.*, **33**, 245–261, https://doi.org/10.1175/JTECH-D-15-0159.1.

Maresca, J. W., Jr., and T. M. Georges, 1980: Measuring RMS wave height and the scalar ocean wave spectrum with HF skywave radar. *J. Geophys. Res.*, **85**, 2759–2771, https://doi.org/10.1029/JC085iC05p02759.

Mentaschi, L., G. Besio, F. Cassola, and A. Mazzino, 2013: Problems in RMSE-based wave model validations. *Ocean Modell.*, **72**, 53–58, https://doi.org/10.1016/j.ocemod.2013.08.003.

Middleditch, A., 2013: Spatiotemporal spectral averaging of high frequency radar wave data. ACORN Rep. 2013-3, 45 pp., http://imos.org.au/fileadmin/user_upload/shared/ACORN/reports/2013-3-Spatiotemporal-Spectral-Averaging-of-High-Frequency-Radar-Wave-Data.pdf.

Paduan, J. D., and L. K. Rosenfeld, 1996: Remotely sensed surface currents in Monterey Bay from shore-based HF radar (Coastal Ocean Dynamics Application Radar). *J. Geophys. Res.*, **101**, 20 669–20 686, https://doi.org/10.1029/96JC01663.

Phillips, O. M., 1966: *The Dynamics of the Upper Ocean*. Cambridge University Press, 261 pp.

Pingree, R. D., 1980: Physical oceanography of the Celtic Sea and English Channel. *The North-West European Shelf Seas: The Sea Bed and the Sea in Motion II. Physical and Chemical Oceanography, and Physical Resources*, F. T. Banner, M. B. Collins, and K. S. Massie, Eds., Elsevier Oceanography Series, Vol. 24, 415–465, https://doi.org/10.1016/S0422-9894(08)71358-8.

Quentin, C. G., 2002: Etude de la surface océanique, de sa signature radar et de ses interactions avec les flux turbulents de quantité de mouvement dans le cadre de l'experience FETCH (in French). Ph.D. thesis, Université Pierre et Marie Curie, 264 pp., https://tel.archives-ouvertes.fr/tel-00010934/document.

Ramos, R. J., H. C. Graber, and B. K. Haus, 2009: Observation of wave energy evolution in coastal areas using HF radar. *J. Atmos. Oceanic Technol.*, **26**, 1891–1909, https://doi.org/10.1175/2009JTECHO631.1.

Saviano, S., A. Kalampokis, E. Zambianchi, and M. Uttieri, 2019: A year-long assessment of wave measurements retrieved from an HF radar network in the Gulf of Naples (Tyrrhenian Sea, Western Mediterranean Sea). *J. Oper. Oceanogr*, **12**, 1–15, https://doi.org/10.1080/1755876X.2019.1565853.

Shen, C., E. Gill, and W. Huang, 2012: Simulation of HF radar cross sections for swell contaminated seas. *Oceans 2012*, Hampton Roads, VA, IEEE, 1–5, https://doi.org/10.1109/OCEANS.2012.6404836.

Stewart, R. H., 1971: Higher order scattering of radio waves from the sea. *1971 Antennas and Propagation Society Int. Symp.*, Los Angeles, CA, IEEE, 190–193, https://doi.org/10.1109/APS.1971.1150935.

——, and J. R. Barnum, 1975: Radio measurements of oceanic winds at long ranges: An evaluation. *Radio Sci.*, **10**, 853–857, https://doi.org/10.1029/RS010i010p00853.

Tracy, B., E. Devaliere, J. Hanson, T. Nicolini, and H. Tolman, 2007: Wind sea and swell delineation for numerical wave modeling. *10th Int. Workshop on Wave Hindcasting and Forecasting and Coastal Hazards Symp.*, Oahu, HI, WMO/IOC Joint Technical Commission for Oceanography and Marine Meteorology, P12, http://www.waveworkshop.org/10thWaves/Papers/10th_wave_paper_tracy_dhnt.pdf.

Voulgaris, G., N. Kumar, K.-W. Gurgel, J. C. Warner, and J. H. List, 2011: 2-D inner-shelf current observations from a single VHF WEllen RAdar (WERA) station. *2011 IEEE/OES 10th Current,*

Waves and Turbulence Measurements, Monterey, CA, IEEE, 57–65, https://doi.org/10.1109/CWTM.2011.5759525.

Wang, W., P. Forget, and C. Guan, 2014: Inversion of swell frequency from a 1-year HF radar dataset collected in Brittany (France). *Ocean Dyn.*, **64**, 1447–1456, https://doi.org/10.1007/s10236-014-0759-9.

——, ——, and ——, 2016: Inversion and assessment of swell wave heights from HF radar spectra in the Iroise Sea. *Ocean Dyn.*, **66**, 527–538, https://doi.org/10.1007/s10236-016-0941-3.

Weber, B. L., and D. E. Barrick, 1977: On the nonlinear theory for gravity waves on the ocean's surface. Part I: Derivations. *J. Phys. Oceanogr.*, **7**, 3–10, https://doi.org/10.1175/1520-0485(1977)007<0003:OTNTFG>2.0.CO;2.

Wyatt, L. R., 1986: The measurement of the ocean wave directional spectrum from HF radar Doppler spectra. *Radio Sci.*, **21**, 473–485, https://doi.org/10.1029/RS021i003p00473.

——, 1990: A relaxation method for integral inversion applied to HF radar measurement of the ocean wave directional spectrum. *Int. J. Remote Sens.*, **11**, 1481–1494, https://doi.org/10.1080/01431169008955106.

——, 1999: HF radar measurements of the development of the directional wave spectrum. *The Wind-Driven Air-Sea Interface*, M. L. Banner, Ed., School of Mathematics, University of New South Wales, 433–440.

——, 2000: Limits to the inversion of HF radar backscatter for ocean wave measurement. *J. Atmos. Oceanic Technol.*, **17**, 1651–1666, https://doi.org/10.1175/1520-0426(2000)017<1651:LTTIOH>2.0.CO;2.

——, 2002: An evaluation of wave parameters measured using a single HF radar system. *Can. J. Remote Sens.*, **28**, 205–218, https://doi.org/10.5589/m02-018.

——, 2005: HF radar for coastal monitoring—A comparison of methods and measurements. *Europe Oceans 2005*, Brest, France, IEEE, 314–318, https://doi.org/10.1109/OCEANSE.2005.1511732.

——, 2017: Wave power measurements in the Celtic Sea using HF radar. *OCEANS 2017-Aberdeen*, Aberdeen, United Kingdom, IEEE, 1–4, https://doi.org/10.1109/OCEANSE.2017.8084723.

——, J. J. Green, A. Middleditch, M. D. Moorhead, J. Howarth, M. Holt, and S. Keogh, 2006: Operational wave, current, and wind measurements with the Pisces HF radar. *IEEE J. Oceanic Eng.*, **31**, 819–834, https://doi.org/10.1109/JOE.2006.88838.

——, ——, ——, ——, ——, ——, and ——, 2009: Signal sampling impacts on HF radar wave measurement. *J. Atmos. Oceanic Technol.*, **26**, 793–805, https://doi.org/10.1175/2008JTECHO614.1.

——, ——, and ——, 2011: HF radar data quality requirements for wave measurement. *Coast. Eng.*, **58**, 327–336, https://doi.org/10.1016/j.coastaleng.2010.11.005.

Young, I., and L. Verhagen, 1996: The growth of fetch limited waves in water of finite depth. Part 1. Total energy and peak frequency. *Coast. Eng.*, **29**, 47–78, https://doi.org/10.1016/S0378-3839(96)00006-3.

Zhang, J., and E. W. Gill, 2006: Extraction of ocean wave spectra from simulated noisy bistatic high-frequency radar data. *IEEE J. Oceanic Eng.*, **31**, 779–796, https://doi.org/10.1109/JOE.2006.886201.